Low Field Magnetic Resonance Imaging of the Eye

Inexpensive MRI for Ocular Conditions

Corné Haasjes

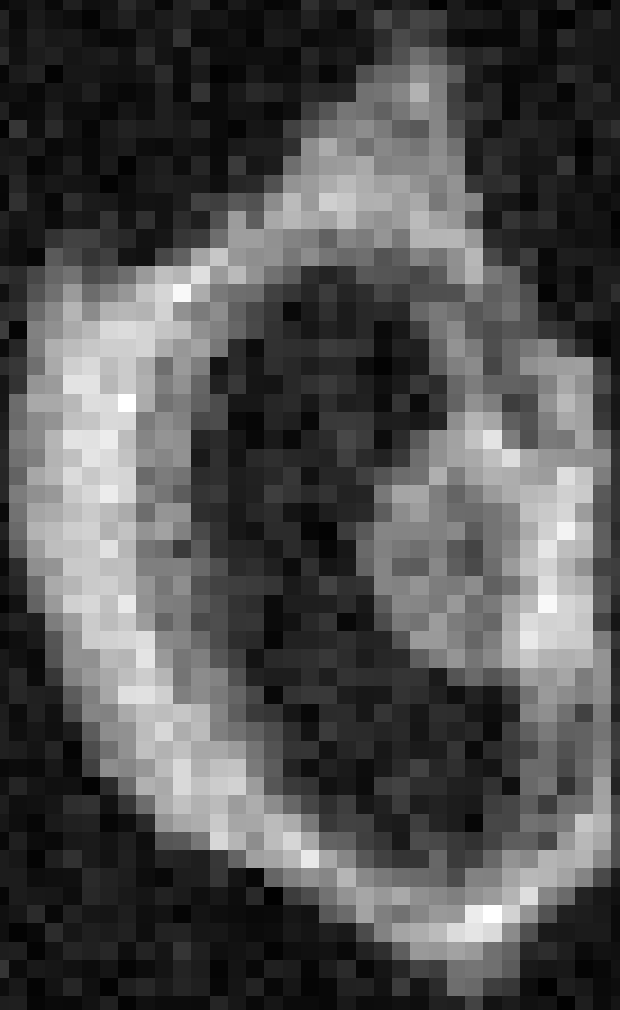

TU Delft

LUMC Leids Universitair Medisch Centrum

Low Field Magnetic Resonance Imaging of the Eye

Inexpensive MRI for Ocular Conditions

by

Corné Haasjes

to obtain the degree of Master of Science
at the Delft University of Technology,
to be defended publicly on Thursday December 1, 2022 at 2:45 PM.

Student number:	4698495	
Project duration:	January 1, 2022 – December 1, 2022	
Thesis committee:	Dr. ir. R. F. Remis,	TU Delft, supervisor
	Dr. J. W. M. Beenakker,	LUMC, supervisor
	Prof. dr. ir. J. L. Herder,	TU Delft
	Dr. F. M. Vos,	TU Delft

Cover:	T_1-weighted low field MRI scan of a porcine eye.
Style:	TU Delft Report Style, with modifications by Daan Zwaneveld and Corné Haasjes

An electronic version of this thesis is available at `http://repository.tudelft.nl/`.

TU Delft

LUMC Leids Universitair Medisch Centrum

Preface

This thesis is probably the last thing I wrote as a student, and thus in a sense concludes my study period. During the past two years and three months, I spent a large amount of my time learning how physics can be used for medical purposes. A significant portion of this period consisted of my internship, literature study and graduation project. During my internship, I developed a pipeline for semi-automatic, accurate localisation of tantalum clips that are used for proton beam therapy planning. This pipeline could be incorporated in an image-based treatment planning system. My internship project thus focused on the treatment planning stadium, where MRI has already proven its use. My graduation project focused on a possible application of MRI in the early diagnostic stadium, which is currently dominated by ultrasound. This project did not include much image processing, but there was a lot to learn about MRI physics and hardware. Thanks to the low field scanner, I had the opportunity to work with MRI at a completely different level than I had done before. Alongside this project, I worked on a literature study about the physics and applications of ultrasound imaging in ocular oncology, which was helpful in defining the research problem and design requirements for my graduation project.

I am grateful for the support and guidance which I received from many people during this project. First of all, I would like to thank Jan-Willem Beenakker and Rob Remis for supervising me. Our (ir)regular meetings helped me to look more critically at the results, determine the direction of the project, and to work on my weaker points concerning the general scientific process. Thank you for all your advice regarding my literature study, which stimulated me to broaden my view, and also exposed my bias towards MRI. I also want to thank Andrew Webb for giving me the opportunity to work in his lab. Thanks, Javad, for all your help with building the eye coils and other hardware related parts of my project. Thanks also for preventing me from blowing things up. Chloé, thank you for helping me with scanning, and for having the patience to let me do most things myself. Without you I would probably know a lot less about the acquisition side of the low field scanner. Finally, I would like to thank all members of the MReye group and the low field group. Your advice during the (bi-)weekly meetings definitely helped me to look at my work from different perspectives.

Corné Haasjes
Bodegraven, November 2022

Summary

Ultrasound imaging is an important modality in ocular oncology, allowing for fast examination of the eye by the ophthalmologist themselves. It is clinically used to measure tumour sizes for treatment planning. However, ocular ultrasound is limited to two-dimensional imaging, and suffers from poor contrast between tumour and sclera, which negatively impacts the accuracy of tumour measurements. In this work, low field MRI is investigated as a possible alternative for ultrasound imaging. Design requirements are a scan time of less than 4 minutes; resolution of 1.0 mm isotropic; Field of View (FOV) large enough to contain the eye and the orbit; contrast sufficient to distinguish the sclera, vitreous, tumour, lens and lipid. The experimental setup consists of a 46 mT Halbach-array based scanner, a volume coil as transmit coil and a custom-built surface coil as receive coil. Images are made of a water phantom to characterise the FOV, and a porcine eye to characterise the contrast. The FOV is found to meet the requirements, and the contrast is sufficient to distinguish the sclera, vitreous, lens and lipid in porcine eyes. The resolution is too low and the scans take too long (about 5 minutes at a resolution of 1.0 × 1.0 × 7.5 mm). Increasing the resolution and decreasing the scan time will result in a low Contrast to Noise Ratio (CNR), causing the contrast requirement to be violated. Fast, high-resolution three-dimensional imaging is therefore not feasible on the current system. The CNR can be improved by using a higher field strength, which requires the development of new hardware. Furthermore, in order to develop a clinically useable system, it is necessary to determine tumour contrast, design optimised pulse sequences, and test the method on human subjects.

Contents

Nomenclature

Abbreviations

Abbreviation	Definition
CNR	Contrast to Noise Ratio
(D)CE-MRI	(Dynamic) Contrast Enhanced MRI
ETL	Echo Train Length
FOV	Field of View
GRE	Gradient Recalled Echo
MRI	Magnetic Resonance Imaging
PD	Proton Density
RF	Radio Frequency
Rx coil	Receive coil
TSE	Turbo Spin Echo
Tx coil	Transmit coil
UM	Uveal Melanoma
SNR	Signal to Noise Ratio

Symbols

Symbol	Definition	Unit
C_M	Matching capacity	[pF]
C_T	Tuning capacity	[pF]
B_0	Static magnetic field	[T]
B_1	Radiofrequency field	[T]
B_1^+	Transmitted radiofrequency field	[T]
$M_\perp$	Transverse magnetisation	[A m^2]
M_z	Longitudinal magnetisation	[A m^2]
N_{avg}	Number of averages	[-]
T_1	Longitudinal relaxation time	[ms]
T_2	Transverse relaxation time	[ms]
T_2'	Reversible transverse relaxation time	[ms]
T_2^*	Effective transverse relaxation time	[ms]
TE	Echo time	[ms]
TE_{eff}	Effective echo time	[ms]
TR	Repetition time	[ms]
γ	Gyromagnetic ratio (2.68×10^8 rad/s/T for a hydrogen proton in water)	[rad/s/T]

1 Introduction

Uveal Melanoma (UM) is the most common ocular tumour in western-european adults, and is traditionally evaluated using funduscopy and ultrasound imaging [1]. Unlike optical modalities, ultrasound imaging is not hindered by opaque media and does not suffer from optical deformations. It is therefore an essential imaging modality for the diagnosis and treatment planning of ocular tumours [2]. Ultrasound is relatively inexpensive, it is fast enough to allow for real-time imaging, and the examination can be performed by the ophthalmologists themselves. It is clinically used to assess the location and shape of the tumour, to detect related abnormalities such as retinal detachment and extrascleral extension, and to measure its thickness and basal diameters [2, 3]. These measurements are used for treatment decisions: small tumours (thickness < 7 mm, basal diameter < 16 mm) are usually treated with brachytherapy, larger tumours with proton beam therapy or enucleation. Depending on the treatment, the measurements are also used for treatment planning.

Ocular ultrasound is a widely used modality, but also has some major shortcomings. The equipment used for ocular ultrasound is limited to two-dimensional images, which negatively affects the accuracy of tumour size measurements [4, 5]. Furthermore, the contrast between some structures in the eye is low, e.g. it is hard to distinguish the sclera from a tumour [6]. Additionally, ultrasound is less sensitive to retinal detachment and extrascleral extension than Magnetic Resonance Imaging (MRI) [7, 8]. Finally, ultrasound images are relatively noisy. This is why ocular MRI is nowadays becoming increasingly important for tumour diagnosis and treatment planning. With MRI, three-dimensional images can be acquired, allowing for more accurate tumour measurements in some cases [3]. MR images also exhibit excellent contrast, and with Dynamic Contrast Enhanced (DCE) MRI it is possible to perform functional imaging of the eye. However, due to its high costs and long acquisition times, MRI is not used for the first examinations of potential eye tumours. These examinations are therefore still performed with ultrasound.

The high costs of MRI are primarily caused by the use of a strong magnetic field. This has led to the development of low field MRI. In the LUMC, a system is being developed with a static field strength of 0.5 mT, instead of the 1.5 or 3 T used in clinical MRI systems [9]. These developments have resulted in a relatively inexpensive and mobile system, which could for example be used in the ophthalmology department. Ideally, a low field system for ophthalmology should be able to acquire three-dimensional images of the eye, with good contrast between the different eye tissues. In this work, the feasibility of such a system is investigated.

A low field MRI scanner for ocular conditions would introduce three-dimensional imaging early in the diagnostic process, but could also contribute to patient well-being and increase the efficiency of the diagnosis and follow-up process. Ultrasound imaging is strongly dependent on the expertise of the observer, and is therefore only performed by experienced ophthalmologists [10]. The ophthalmologist is therefore responsible for imaging for diagnosis, treatment planning and follow-up. The patient thus needs to regularly visit the ophthalmologist, over a period of several years. In the Netherlands, where diagnosis and

treatment of UM are concentrated in only a few centers, this can be quite demanding for the patient. Using a low field scanner, the imaging can be performed by other staff members. This would shorten the consultation time for the ophthalmologist, while imaging can still be performed immediately after the consult. Moreover, imaging can be partly outsourced to referral institutions, especially during follow-up. This further reduces the workload for the ophthalmologist, and is also less demanding for the patient.

1.1. Anatomy and MRI of the eye

The flexibility of MRI allows to design an imaging protocol specifically for the eye. This requires knowledge about the tissues in the eye and their behaviour on MRI scans. A schematic diagram of the anatomy of the eye is shown in Figure 1.1, as well as ultrasound and MRI images.

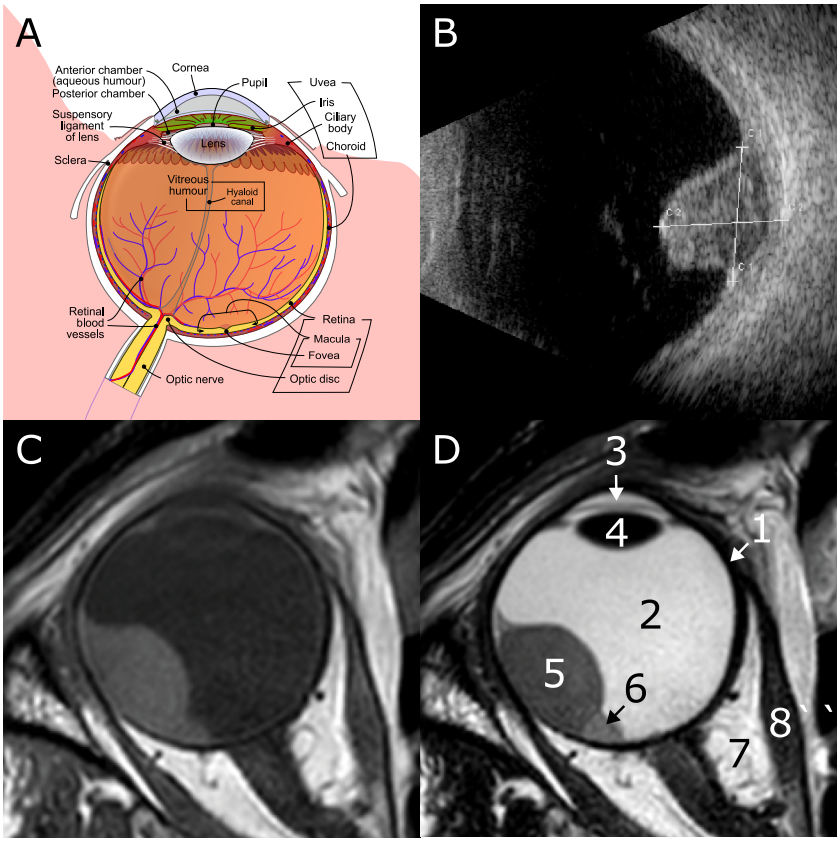

Figure 1.1: Schematic diagram (**A**), ultrasound (**B**) and MRI (**C, D**) images of the human eye. **A**: The anterior segment includes the cornea, anterior chamber, iris, ciliary body, posterior chamber and lens. The posterior segment includes the sclera, choroid, retina and vitreous humour. The sclera can be easily distinguished on the MRI images, but not on the ultrasound image (**B**). The MRI images are T_1-weighted (**C**) and T_2-weighted (**D**). In image **D**, various structures are highlighted. The sclera (1) is dark on both T_1 and T_2-weighted scans. The vitreous (2) and aqueous (3) humour have a relatively high intensity on T_2-weighted scans, but exhibit low signal intensity on T_1-weighted scans. The lens (4) is dark on both scans; on the T_1-weighted scan, it is slightly hyperintense to the vitreous. The tumour (5) has a low to medium intensity on the T_2-weighted image and a high intensity on the T_1-weighted image. In this case, retinal detachment (6) can only be distinguished from the tumour in the T_2-weighted scan. Lipid (7) is bright on both scans, and muscles (8) are dark on both scans. **A** from [11], **B** adapted from [12], and **C, D** from [8].

The human eye is approximately spherical, with a diameter of circa 24 mm [13]. The eye is divided into an anterior and a posterior segment; these segments are separated by the crystalline lens [14]. The wall of the eye consists of three layers. The outer layer is a fibrous layer, composed of collagen, and responsible for the eye shape. The anterior part of this layer is the transparent *cornea*, which is about 0.5 mm thick.

The posterior and largest part is the white *sclera*, which has a thickness of 0.3 - 1.0 mm. Both layers exhibit a low signal intensity on MRI scans [2].

Inside this fibrous layer, a vascular layer called the uvea is found. The posterior part of this layer is the *choroid*, a vascular layer that supplies blood to the other layers of the eye. In the anterior segment, the choroid becomes the ciliary body. The ciliary body is ring-shaped and encircles the lens. The *iris* is the most anterior part of the vascular layer. On MRI scans, the vascular layer exhibits various intensities depending on the pulse sequence and contrast enhancement, but it is generally hyperintense to the sclera.

The *retina* is the inner layer of the eye wall; this layer is only present in the posterior segment. It contains photoreceptors that are necessary for vision. The retina is relatively thin: its thickness ranges from 0.056 to 0.1 mm [15]. On MRI scans, the retina cannot be distinguished from the choroid; depending on the pulse sequence, either the choroid or the retina will be visible.

A large part of the posterior segment is filled with the *vitreous humour* or vitreous body, a gel-like transparent fluid. The vitreous humour consists for a large part of water, and therefore behaves similar to free water on MRI scans. As a result, its relaxation times are relatively long, i.e. on the order of seconds for both T_1 and T_2 [16]. The anterior segment also contains two cavities: the *anterior chamber* between the cornea and the iris, and the *posterior chamber* behind the iris. These chambers are filled with the aqueous humour. In terms of MRI contrast, the signal intensity of the aqueous humour is close to that of the vitreous humour. The *lens* consists mostly of transparent proteins, and has a low intensity on T_2-weighted images and intermediate intensity on T_1-weighted images.

Uveal melanoma originates in most cases from the choroid and grows into the vitreous body [2]. UM can be flat, dome shaped or mushroom shaped, and can be pigmented as well as amelanotic. Pigmented UM is bright on T_1-weighted images and dark on T_2-weighted images. Amelanotic has a medium brightness on both weightings. UM may also have multiple partitions with different pigmentations. The intensity of retinal detachment is close to that of the vitreous, unless it is haemorrhagic; in that case, it is bright on T_2-weighted images. However, retinal detachment cannot be diagnosed with certainty without using contrast-enhanced MRI.

The eye is located in a cavity in the skull called the *orbit*. Apart from the eye itself, this cavity contains lipid, the optical nerve, blood vessels and muscles that control eye movement. On MRI scans, the eye muscles are dark on both T_1 and T_2-weighted images. Lipid is bright on both weightings.

1.2. Design requirements

Since the goal of this project is to study the feasibility of a low field system that can substitute ultrasound in ocular oncology, it is necessary to define requirements that the final result should fulfil. This does not mean that the low field system should have exactly the same properties as an ultrasound imaging system; some of the advantages of ultrasound can be exchanged for benefits of MRI. For example, ultrasound images are acquired much faster, but the higher acquisition times of MRI are acceptable, because MR images are three-dimensional and generally exhibit better contrast than ocular ultrasound [17].

The requirements maintained during this project are listed in Table 1.1. The time limit of 4 minutes is strict and should not be exceeded. Ultimately, patients should be scanned without anaesthesia, and minimise their eye movements in order to prevent motion artefacts. Longer scan times are therefore likely to result in more motion artefacts, which should be avoided. The value of 4 minutes is based on clinical experience and the scan times from the protocol used on 3-Tesla MRI scanners [1]. With a resolution of 1.0 mm isotropic, a reproducibility of 0.5 mm can be achieved. This is an improvement over the reproducibility of tumour measurements on ultrasound images, which is 0.6 mm [18, 19]. The requirements for image contrast are qualitative; there are many different possible contrasts, and it is not realistic to define a hard limit at which certain structures cannot be distinguished anymore.

Although these requirements are met by clinical MRI, it may not be easy to fulfil them using low field MRI. The Signal to Noise Ratio (SNR) of MRI images increases with the field strength; therefore, a lower SNR is inherent to low field MRI. The SNR can be increased by decreasing the resolution or increasing

Parameter	Requirement	Reason
Scan time	Less than 4 minutes	Minimise motion artefacts
Resolution	Less than 1.0 mm isotropic	Higher reproducibility than ultrasound
Field of View	Large enough to contain the eye and orbit	
Contrast / CNR	Sufficient to distinguish the main eye tissues: sclera, vitreous, tumour, lipid and lens	

Table 1.1: Requirements for an ocular low field MRI system. The table also lists reasons for requirements that are not self-explanatory. CNR = Contrast to Noise Ratio.

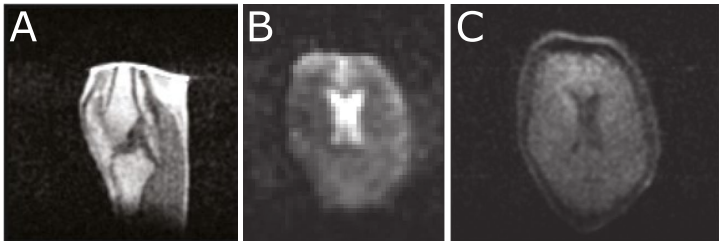

Figure 1.2: Examples of low field MR images of different anatomies: sagittal slice of the knee (**A**), T_1-weighted (**B**) and T_2-weighted images of the brain. Adapted from [21].

the number of averages. The requirements on scan time and resolution therefore implicitly limit the SNR and thus the Contrast to Noise Ratio (CNR). Using the dependency of the SNR on field the strength B_0, the expected SNR loss can be estimated. At low field strengths, the SNR is proportional to $B_0^{3/2}$ [20], and at high field strengths the SNR is approximately proportional to B_0. If the transition from low to high field is assumed to be at 1 T, the SNR decreases by a factor of about 300 when going from 3 T to 50 mT. A fast three-dimensional T_1-weighted scan of the eye in the clinical protocol has a resolution of 0.6 × 0.6 × 2.0 mm and takes about 25 seconds [3]. On the low field scanner, the scan time can be increased to 4 minutes, resulting in an SNR gain of $\sqrt{8}$. Furthermore, the voxel size can be increased to 1.0 mm isotropic. Assuming that the full scan time is used for sampling, this increases the signal per voxel by a factor of 1.4. Lastly, the CNR between tumour and vitreous is about 30, but a CNR of 2 is sufficient to distinguish between these tissues. A signal loss of a factor of 15 is therefore acceptable. In total, this compensates for a signal loss of approximately a factor of 65; the remaining loss amounts to a factor of 5. This result means that the SNR of the low field images can be expected to be lower than required. However, a possible signal increase due to a shorter T_1 as low field strength is not taken into account. Moreover, the estimation is based on a single scan, which has been acquired using an unoptimised sequence, and the result is affected by the use of a contrast agent. With the estimated order of magnitude, it might therefore still be possible to get results that meet the design requirements, for example by optimisation of the pulse sequences. Furthermore, results obtained on other anatomies are encouraging (Figure 1.2), which is another incentive to investigate the feasibility of low field MRI for ocular conditions.

2 Theory

The quality of MR images is affected by various hardware and imaging related aspects. Radio frequency (RF) coils and the Signal to Noise Ratio are two of these aspects that are relevant to this work.

2.1. Principles of coil design

MRI creates images by exciting proton spins in a strong magnetic field. These spins start to precess, which on a macroscopic level causes a rotating magnetisation. This rotating field induces a voltage in the coil, which forms the actual MRI signal. Coils are therefore indispensable for MRI: no images can be obtained without them. Instead of taking a one-size-fits-all approach, it is customary to optimise the coils for a specific application, in this case imaging the eye. This allows to have a good sensitivity at the organ of interest, and to use a smaller FOV, which reduces scan times. The various types of MRI coils can be broadly categorised as volume coils and loop coils [22, 23]. *Volume coils* encompass the full body or a part of the body, e.g. the head or a limb. They are typically cylindrical and generate a relatively homogeneous magnetic field. *Surface coils* consist of one or more loops of wire that are located at the surface of the human body, close to the organ of interest. These coils have a limited penetration depth, which allows to keep the FOV small and thus shorten the acquisition time. However, their magnetic field is inhomogeneous and decreases as a function of depth. If only a surface coil is used, this signal decrease is caused by two effects. First, the transmitted field B_1^+ is inhomogeneous, causing the flip angle to decrease over depth. Second, the sensitivity of the coil decreases over the distance from the coil, which means that the same magnetic field at a larger depth will generate a weaker signal. The first effect can be mitigated by using separate transmit and receive coils. In this case, a volume coil with a homogeneous transmit field can be used to excite the spins. This causes the flip angle to be approximately constant over the whole volume, which effectively increases the penetration depth of the receive coil.

When designing and building a coil, a number of factors should be optimised in order to maximise the received signal. These factors are the tuning and matching of the coil, the quality factor, and coupling; they will be discussed in the next sections.

2.1.1. Tuning and matching

During an MRI scan, the proton spins precess at the Larmor frequency

$$\omega_0 = \gamma B_0, \tag{2.1}$$

where γ is the gyromagnetic ratio andB_0 the static magnetic field of the scanner. This frequency is thus dependent on the magnetic field, and it is necessary that the coil resonates at the same frequency in order to maximise the received signal. If the coil resonates at a different frequency, the signal amplitude will be

lower, resulting in a lower SNR. The process of adjusting the resonance frequency of a coil is called *tuning*. This is done by adding a tuning capacitor C_T parallel to the coil (Figure 2.1). The value of C_T determines the resonance frequency of the resulting LC circuit; C_T is therefore chosen such that the coil resonates at the Larmor frequency.

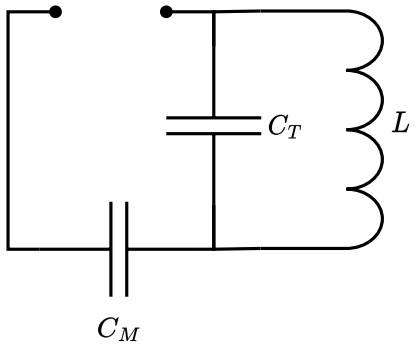

Figure 2.1: Circuit diagram of a coil as used in this work. The tuning capacitor C_T controls the resonance frequency of the coil L. The matching capacitor C_M is used to change the impedance of the circuit to 50 Ω.

During imaging, the induced signal is transmitted to a spectrometer through a transmission line. The transmission line has a specific impedance Z_{cable}, usually of 50 Ω. This impedance can be different from the coil impedance, Z_{coil}. If there is a difference between Z_{cable} and Z_{coil}, a part of the power from the coil will be reflected. This fraction is given by the reflection coefficient Γ, defined as

$$\Gamma = \frac{Z_{cable} - Z_{coil}}{Z_{cable} + Z_{coil}}. \tag{2.2}$$

If both impedances are equal, all power is transmitted to the spectrometer and contributes to the measured signal. The coil impedance thus has to be matched to the transmission line impedance; this is called *impedance matching*. If the coil is not well matched, the transmitted signal will be lower. There are various methods of impedance matching, of which only capacitive impedance matching is used in this work. This means that a matching capacitor C_M is added in series with the coil (Figure 2.1). The value of C_M is chosen such that $Z_{coil} = 50\ \Omega$ [22].

2.1.2. Quality factor

Another aspect of an RF coil influencing the SNR and thus the image quality, is the quality factor Q. This factor expresses the ratio between the magnetic field energy stored in the coil and the energy loss during a single cycle, and is defined as

$$Q = \frac{\omega L}{R_{eff}}. \tag{2.3}$$

In this equation, ω is the frequency of the RF pulse, L the inductance of the coil and R_{eff} the effective resistance of the system. For coils with the same size and geometry, the SNR is proportional to $\sqrt{Q}$. The coil resistance is one of the main components of the total resistance R_{eff}, and should therefore be minimised in order to maximise the SNR. In addition to the coil, the sample also contributes to R_{eff}, which means that the quality factor changes once the sample is introduced in the scanner. This is called the loading effect. Depending on the static field strength and the characteristics of the coil, the loading effect may have a significant effect on the quality factor and the tuning and matching of the coil [24].

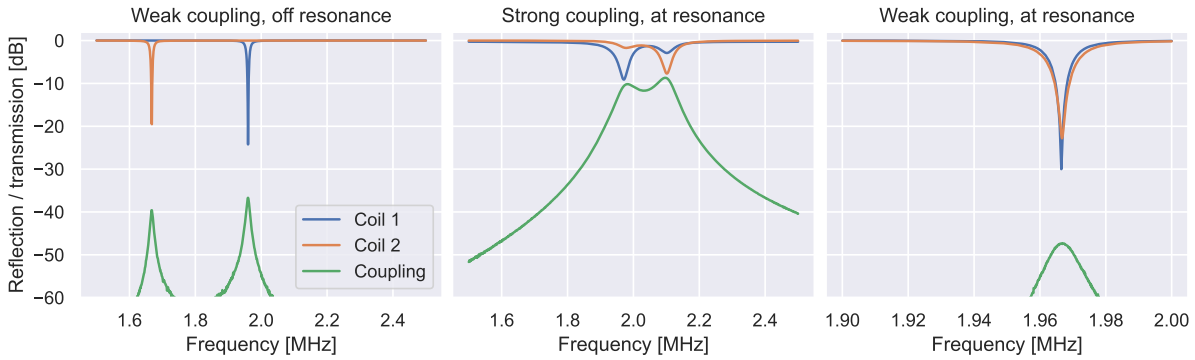

Figure 2.2: Example of coupling between two coils. Each graph displays the fraction of the power reflected by each coil (reflection) and the fraction of the power transmitted from one coil to the other (coupling). If the resonance frequencies of both coils differ significantly (left), the coupling is negligible. If the resonance frequencies are close and the coupling is strong (center), the peaks of both coils 'split', i.e. they resonate at multiple frequencies. If two coils with the same resonance frequency (right) are properly positioned with respect to each other, the coupling can be very low. The left and right figures are made using the setup described in Section 3.1; the center figure is made using two coils that have not been used in this work.

2.1.3. Coupling

When multiple coils are located close to each other, they will interact. This interaction is called *inductive coupling*, which means that the magnetic field caused by a current in one coil will induce a current in the other coils. Coupling causes a shift in the resonance frequency of the coils, changes the bandwidth of the coils, and can cause the coil to resonate at multiple frequencies (Figure 2.2). When two coils are used in MRI, for example by using separate transmit and receive coils, coupling is likely to cause problems. During the transmit phase, the transmitted pulse will immediately induce a current in the receive coil, which may damage the equipment. Furthermore, coupling affects the homogeneity of the transmit field [23]. It is therefore necessary to reduce or eliminate the coupling. One way to reduce the coupling, is to position the coils with their magnetic fields perpendicular to each other; this approach is followed in this work. If an orthogonal setup is not possible, a detuning circuit can be added to the receive coil. This circuit changes the resonance frequency of the receive coil during the transmit phase, thus preventing the receive coil to resonate with the RF pulse [22].

2.2. Signal to Noise Ratio

Noise is a major factor determining image quality, and is visible in the image as random fluctuations in the signal intensity. In the ideal case, noise in MRI originates primarily from random fluctuations in the receive coil and the sample, but it can also originate from the equipment and from external sources. At high field strengths, noise is dominated by the sample; at low field strengths, the coil noise is dominant, although high-Q coils can get close to sample dominance. Noise is usually characterised in terms of the Signal to Noise Ratio (SNR). This ratio is defined as SNR $= S/\sigma$, with S the signal strength and σ the standard deviation of the noise [25].

Since noise is a random process, a straightforward way to increase the SNR is to acquire multiple averages. The SNR per voxel is then proportional to the square root of the number of averages N_{avg}, i.e. SNR/voxel $\propto \sqrt{N_{avg}}$ [24].

The SNR also depends on other imaging parameters. For example, the field of view and resolution affect the amount of signal acquired per voxel, and therefore the SNR. In this work, the most important case is a change of resolution, while keeping the field of view constant. In the readout direction, this can be accomplished without changing the readout gradient strength and dwell time. Although this will increase the sampling time, this does not affect the acquisition time, because the repetition time is generally much longer than the sampling time. When this approach is followed, the SNR is approximately proportional to the inverse square root of the readout resolution. This proportionality is not exact, because an increase

in sampling time also increases the minimum possible echo time. This leads to changes in the sampled signal, and therefore in the SNR. Increasing the resolution in the phase encoding directions will increase the acquisition time. In this case, the SNR is also proportional to the inverse square root of the resolution, and the acquisition time scales linearly with the resolution [24].

Even more important than the SNR is the Contrast to Noise Ratio (CNR). The CNR between two tissues is defined as the signal difference between these tissues, divided by the standard deviation of the noise [24]. A high CNR means that two tissues can be easily distinguished from each other. Contrast depends strongly on the pulse sequence, and the contrast between two tissues can be simulated if the relaxation times of these tissues are known. These simulations are explained in Appendix C, as well as a problem that occurred when simulating multiple repetitions of the same sequence. However, these simulations were ultimately not used, because other problems were more urgent than poor contrast between the tissues in the eye.

3 Method

3.1. Experimental setup

The largest part of the experimental setup used for this work did already exist. All experiments are performed on a low field MRI scanner, designed and built by O'Reilly, De Vos, Teeuwisse and Webb et al. [9, 26, 27, 21]. The static magnetic field of this scanner is produced by a Halbach array of permanent magnets (Figure 3.1), and has a strength of 46 mT. The scanner has a resonance frequency of approximately 1.97 MHz. Unlike conventional MRI scanners, the field of a Halbach array is not oriented along the bore of the scanner. Instead, it is oriented perpendicular to the bore; the orientations of the anatomical axes for the system used in this work are explained in Table 3.1. Furthermore, for some experiments a transmit solenoid with a diameter of 20 cm is used; this solenoid is characterised in [9]. In addition to this hardware, a surface coil is designed for imaging the eye, as described in Section 3.2. An eye coil holder is 3D-printed to fix the position of this coil with respect to the solenoid and the sample. This holder is fixed in the center of the transmit solenoid using two adjustable screws; before scanning, its position is slightly adjusted to minimise coupling between the coils. The coupling should not exceed -20 dB. Phantoms are positioned just below the eye coil. A picture of the full setup is included in Figure 3.2.

3.2. Coil design

Since the eye is a superficial structure, a surface coil can be used. A surface coil has the obvious disadvantage of an inhomogeneous field, but it also has a limited FOV, allowing to reduce scan times. During

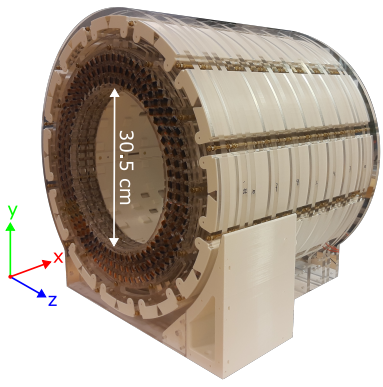

Figure 3.1: Picture of the Halbach array (without the shielding present in Figure 3.2). The coordinate system of the scanner is included in the bottom left. The bore has a diameter of 30.5 cm.

Axis	Anatomical axis
x	foot - head
y	posterior - anterior
z	left - right

Table 3.1: Geometrical and anatomical axes of the low field scanner. As usual, the B_0 field is oriented along the z axis, in this case the left-right direction.

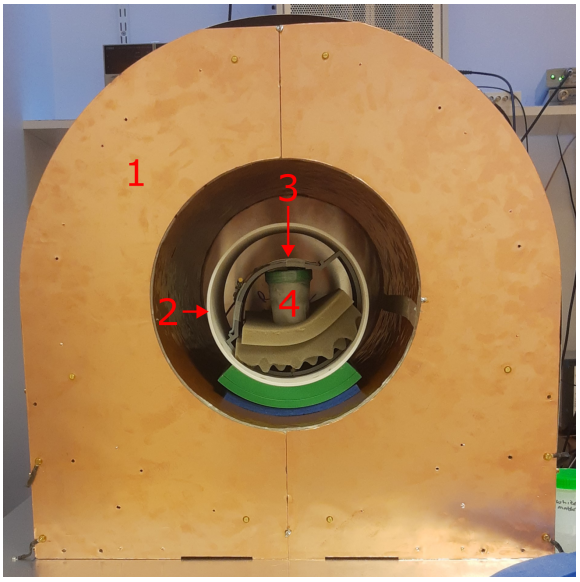

Figure 3.2: Setup for imaging a porcine eye. The picture shows the magnet and gradient assembly **(1)**, with the coil assembly in the center of its bore. The white cylinder is the transmit solenoid **(2)**. The eye coil **(3)** is put on top of a coil holder inside the transmit coil, and the phantom **(4)** is placed inside the coil holder below the eye coil.

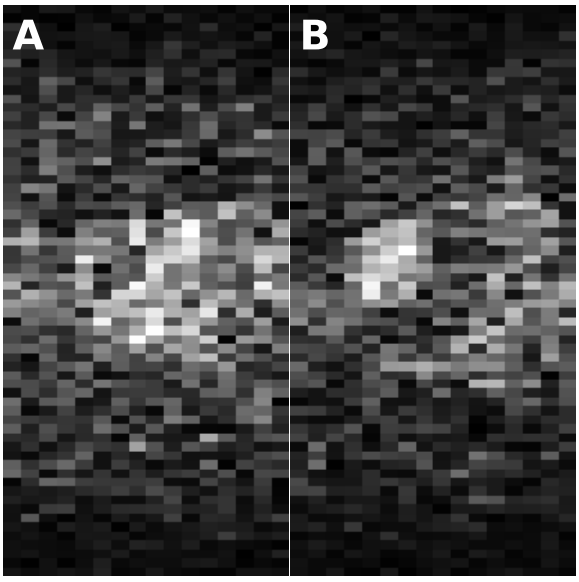

Figure 3.3: T_2 **(A)** and T_1-weighted **(B)** images of a porcine eye acquired during the preliminary experiments (Appendix A). The SNR of these images is low and no structures can be distinguished.

preliminary experiments, an eye coil with dimensions of 4.1 × 5.6 cm was built. Its penetration depth was measured, both with and without a separate transmit coil, and a porcine eye was scanned. More details about these experiments can be found in Appendix A. The penetration depth was found to approximately double when a separate volume coil was used as transmit coil, and all experiments described below therefore use a separate transmit coil. Furthermore, the SNR of the images of a porcine eye was too low (Figure 3.3).

A new eye coil is therefore designed, with a higher Q and larger dimensions to improve the SNR and penetration depth. The coil consists of three loops of 1.5 mm diameter Litz wire with 1500 strands, attached to a curved, plastic base plate (Figure 3.4). The coil shape is a rectangle with a notch to leave some space for the nose. The dimensions of the coil are based on the results of field simulations explained in Appendix B. The tuning and matching capacitors are adjusted iteratively, until the resonance frequency of the coil is equal to to 1.966 MHz, and the input impedance is close to 50 Ω. A variable capacitor is added to the tuning capacitor, to allow the resonance frequency to be adjusted to small changes in the static field strength of the magnet. Further details of the coil are provided in Table 3.2.

Number of loops	3
Largest inner dimensions	60.8 × 70.8 mm
Largest outer dimensions	70.8 × 80.9 mm
C_T	3714 pF
C_M	171.0 pF
Q	180

Table 3.2: Properties of the surface coil used during the experiments. Q was measured in the setup shown in Figure 3.2. C_M and C_T were measured using a Keysight U1773C LCR meter [28].

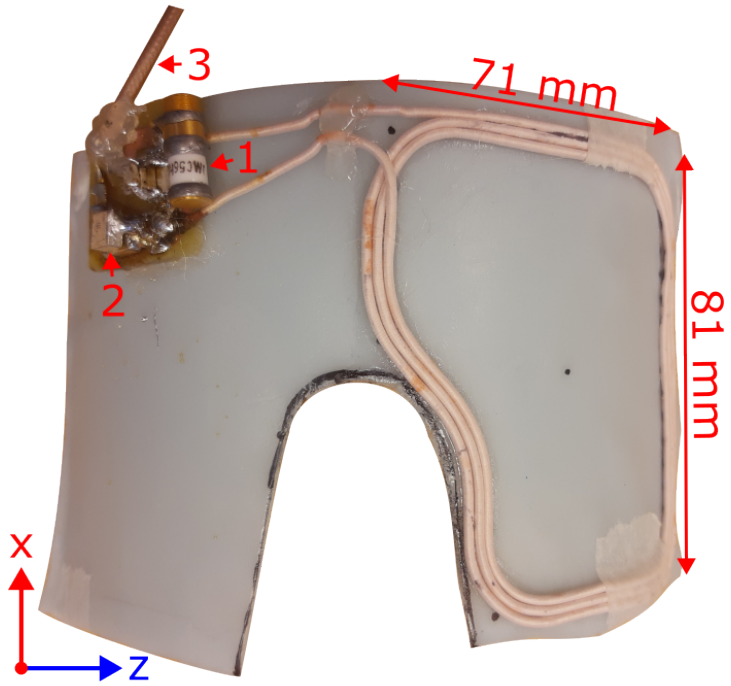

Figure 3.4: Coil prototype used during the experiments. Litz wire is glued onto a plastic base, made from radiotherapy mask material. The coil's outer width (horizontal direction) and height (vertical direction) are indicated by double-headed arrows. The coordinate system of the scanner is indicated in the bottom left. The tuning and matching circuit is located in the top left. This circuit consists of a tuning capacitor **(1)** and a matching capacitor **(2)**, and is connected to the transmission line **(3)**. A variable capacitor with a range of 1 – 30 pF is added to the tuning capacitor, allowing to correct for small variations in the static field strength.

3.3. Experiments

Two experiments are performed: one to characterise the coil sensitivity by determining its penetration depth, and one to assess the performance of the low field system on porcine eyes.

3.3.1. Penetration depth

The penetration depth of the coil is determined using a cylindrical phantom (diameter: 9 cm, length: 19.5 cm) filled with Milli-Q water. The top of the phantom is located approximately 1 cm below the surface coil, and the axis of the phantom is oriented along the bore of the scanner. A 3D Turbo Spin Echo (TSE) scan is made with the following scan parameters: readout/phase 1/phase 2: y/z/x; FOV: 150 × 120 × 250 mm; resolution: 1.0 × 2.0 × 5.0 mm; $TR/TE/TE_{eff}$: 8000 ms/20 ms/20 ms (in-out k-space trajectory); echo train length (ETL): 60. Total scan duration is 00:06:42. A high resolution is chosen for the readout direction, because the penetration depth is determined along this direction.

3.3.2. Imaging a porcine eye

Several scans are made of a porcine eye, in order to assess whether the developed setup meets the requirements outlined in Section 1.2. A porcine eye is used because it is relatively similar to the human eye in terms of anatomy. A phantom is prepared by filling a plastic cup with gauze swabs, with a porcine eye on top of it, the lens facing upward. The rest of the cup is filled with Fluorinert FC-3283 [29]. The cup is placed in the receive-transmit coil assembly, with the top of the eye located approximately 1.5 cm below the surface coil.

Coupling is measured using a Copper Mountain S5048 Vector Network Analyser [30], before the first scan and after the last scan. 3D TSE scans are made with different resolutions and weightings. The parameters used for these scans are shown in Table 3.3. In addition to the TSE scans, a 3D scan with

	Weighting	Resolution [mm]	Averages	$TR/TE/TE_{eff}$ [ms]	ETL	Trajectory	Duration [mm:ss]
TSE 1	PD	1.0 × 1.0 × 4.0	1	1000/12/12	6	in-out	02:32
TSE 2	T_1	1.0 × 1.0 × 7.5	8	500/8/8	6	in-out	05:20
TSE 3	T_2	1.0 × 1.0 × 7.5	8	1500/15/150	20	linear	04:48
TSE 4	T_1	0.67 × 0.67 × 7.5	8	500/12/12	6	in-out	08:00
TSE 5	T_2	0.67 × 0.67 × 7.5	8	1500/15/150	20	linear	07:14
GRE 1	T_1	0.67 × 0.67 × 7.5	1	300/12/12			03:48

Table 3.3: Scan parameters and durations for various scans of a porcine eye. All scans were made with a FOV of 60 × 60 × 60 mm. The readout/phase 1/phase 2 directions are z/y/x. The in-out trajectory samples k-space from center to edges; the linear trajectory samples k-space from bottom to top. PD = Proton Density.

Gradient Recalled Echo (GRE) readout is performed, in order to compare its SNR and acquisition time with the TSE scans. The scan parameters for this scan are also listed in Table 3.3. Most scans were made with 8 slices along the x-direction, in order to decrease the scan time. This was the minimum number of slices necessary to obtain sufficiently detailed images.

3.4. Analysis

3.4.1. Penetration depth

There are various ways to determine the penetration depth; a simple example is fitting an exponential curve to the signal and determining the half-value depth. Although an exponential function does not exactly describe the decay of the coil sensitivity, it works well enough and allows to characterise the penetration depth by a single, interpretable number. A column along the y-axis, located in the center of the coil, is extracted from the image. This column is normalised with respect to its maximum value. If the values are not normalised, the amplitude of the fitted exponential may become extremely large, causing problems with fitting the data. Subsequently, a fit is performed using the model in (3.1). In this model, the signal S is given as a function of the depth d. Furthermore, a is the amplitude of the signal, b is the decay constant and c is the intercept. Although this intercept should ideally be equal to zero, the value of c is expected to be larger than zero due to noise.

$$S(d) = ae^{-bd} + c \tag{3.1}$$

It is not trivial to relate the decay constant b to the penetration depth. Therefore, the half-value depth $d_{1/2}$ is calculated, which is defined as the depth over which the signal amplitude halves:

$$d_{1/2} = \frac{\ln 2}{b} \tag{3.2}$$

In this definition, $d_{1/2}$ is calculated relative to c. The standard deviation in $d_{1/2}$, $\sigma(d_{1/2})$, is calculated from the standard deviation in b as

$$\sigma(d_{1/2}) = \| \frac{\ln 2}{b^2} \| \, \sigma(b). \tag{3.3}$$

3.4.2. Postprocessing

Images were initially reconstructed from the unprocessed k-space data. Additionally, all images were also reconstructed after zero-filling and filtering k-space. With zero-filling, k-space is enlarged by padding it

with zeroes, which results in a higher resolution. The applied filter was a squared sine bell filter, defined as

$$w[k] = 1 - S \cdot \cos^2\left(\frac{\pi}{2}\frac{k - N/2}{N/2}\right), \tag{3.4}$$

with $0 \leq S \leq 1$ the filter strength and N the number of k-space points. This filter suppresses the edges of k-space, which results in suppressed noise in the reconstructed images.

4

Results

4.1. Technical aspects

Two technical aspects of the setup were measured during the experiments: inductive coupling between the receive and transmit coil, and the penetration depth of the eye coil.

4.1.1. Coupling

Plots of the coupling before and after scanning the porcine eyes are shown in Figure 4.1. Before the experiments, the coupling was -47 dB, which is well below the limit of -20 dB. After the experiments, the coupling had increased to -17 dB, which exceeds the limit. The frequencies and reflection peak heights measured before and after the experiments are listed in Table 4.1. The resonance frequencies of the coils shifted a bit: f_0 increased with 1 kHz for the receive coil and 2 kHz for the transmit coil.

	Before experiments		After experiments	
Coil	f_0 [MHz]	Peak height [dB]	f_0 [MHz]	Peak height [dB]
Rx	1.9665	-30	1.9666	-26
Tx	1.9667	-23	1.9669	-20

Table 4.1: Resonance frequencies (f_0) and peak heights for each coil, measured before and after the porcine eye scans. Rx = receive, Tx = transmit.

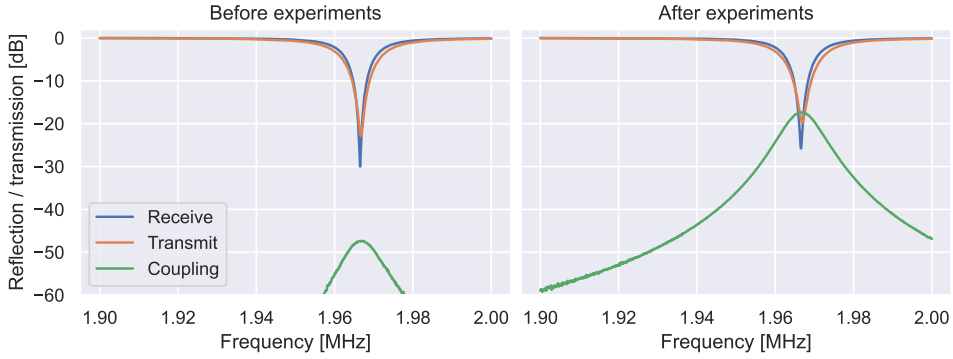

Figure 4.1: Plots of the coupling before the experiments (left) and after the experiments (right). During the measurements, the coupling increased significantly, and the reflection of both coils increased.

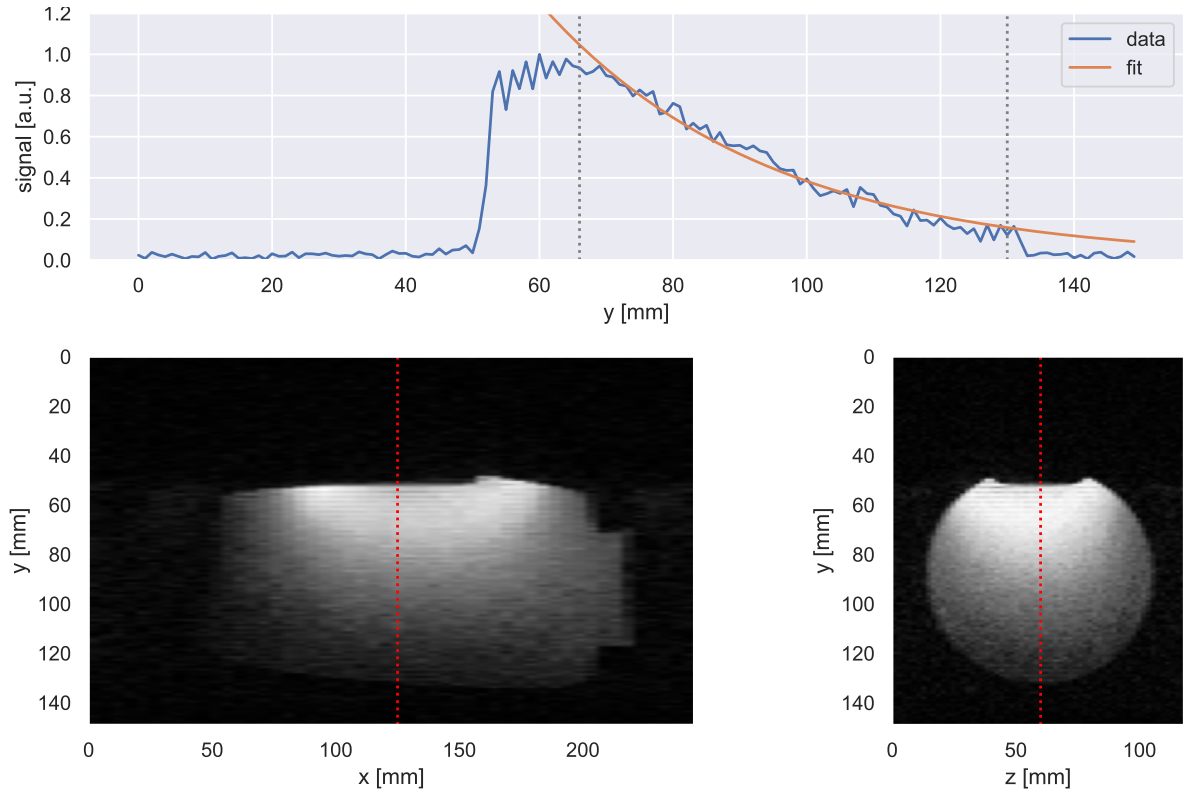

Figure 4.2: Signal profile with fit result (top), a sagittal slice (bottom left) and a transversal slice (bottom right) from an image of the water phantom. The location of the profile is indicated by the red dotted line in the images. The phantom is almost fully visible. The grey dotted lines in the profile indicate the boundaries of the region in which the exponential fit was performed. The coil was located at $y \approx 35$ mm.

4.1.2. Penetration depth

Images of the water phantom and a signal profile fit are shown in Figure 4.2. The fit was only performed in a region where approximately exponential decay was found; the resulting function is

$$S(y) = 7.33e^{-0.03y} + 0.00, \tag{4.1}$$

and the penetration depth $d_{1/2} = 23.50 \pm 2.37$ mm, which is close to the diameter of the human eye. This is 1.7 times the penetration depth obtained with the first coil prototype. The approximately doubled penetration depth can also be qualitatively estimated from the results shown in appendix A.3.1. The current eye coil is able to penetrate the full phantom; the first prototype could penetrate about half the phantom (Figure A.3). The difference between the images is not only caused by the increased coil size, but also by the use of Litz wire and the resulting higher Q. This makes the coil more sensitive, resulting in a higher received signal. The improved field of view, as visible in Figure 4.2, is large enough to image the full eye.

Unlike the signal profile obtained using the first coil prototype, the profile does not only show exponential decay. Between 50 and 70 mm, the signal slightly increases and shows strong oscillations. The oscillations are an artifact caused by the acquisition process. The non-exponential region in the signal profile can be explained using the coil simulations shown in Figure B.2: close to the coil, the signal first increases to a global maximum, and then starts to decrease. The region in which an exponential can be fitted does therefore not start immediately at the coil. Because the water surface is located at a depth of approximately 2 cm from the coil, this behaviour was not visible for the first coil prototype. Due to its larger size, it is visible for the current coil.

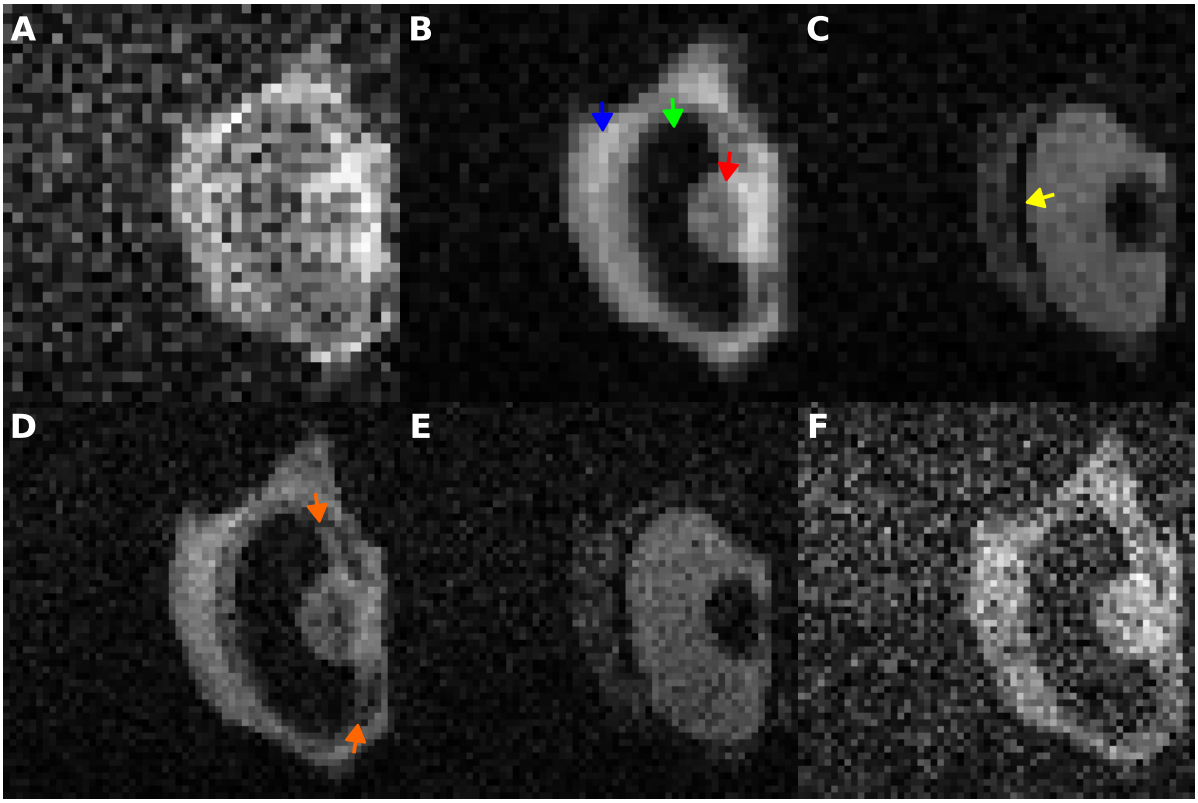

Figure 4.3: Images of a porcine eye, acquired with the six sequences listed in Table 3.3. All images display the center slice of the scans, in the transverse plane; the vertical axis is the readout axis. All images are displayed with the same intensity range. Most structures in the eye can be distinguished in all images, except **A**: the lens (red arrow), vitreous (green arrow) and lipid around the eye (blue arrow). In the T_2-weighted images (**C**, **D**), the sclera is clearly visible (yellow arrow). Furthermore, the high-resolution T_1-weighted image (**E**) visualises some structures around the lens (orange arrows), probably the ciliary body.

4.2. Imaging

The results of the scans listed in Table 3.3 are shown in Figure 4.3. A figure with these results after zero-filling and applying a squared sine bell filter with a strength of 0.2 is included as a supplementary figure (Figure D.1). Due to the zero-filling, the resolution of these images is doubled. Both figures display all images in the same color scale. Certain details in the images are better visible when they are scaled to the full color range; a figure with independently scaled images is included in Figure D.2.

The eye is visible in all images, and the results have improved with respect to the preliminary experiments (Figures 3.3 and A.4). Figure 4.3 A was acquired with a single average and 15 slices along the foot-head direction. The resulting image is noisy and the different structures in the eye can hardly be distinguished. The TR of 1000 ms is in between the values for T_1-weighting and T_2-weighting; the contrast is therefore expected to be in-between T_1 and PD-weighting. The vitreous should then be medium bright, because the TR allows for partial regrowth. This contrast is indeed observed in the image: the lipid is bright, and the vitreous is medium bright, resulting in suboptimal contrast between lipid and vitreous.

Increasing the number of averages and reducing the number of slices should improve the SNR. Figure 4.3 B and C were acquired with 8 averages and 8 slices. Both images show the expected increase in SNR with respect to Figure 4.3 A. Figure 4.3 B was acquired with a short TR and TE_{eff}, which is expected to give a T_1-weighted image (i.e. bright lipid, dark vitreous, and dark to medium bright lens). This T_1-weighting is visible in Figure 4.3 B: the lipid is bright and the vitreous is dark. However, the brightness of the lens and lipid are similar, which was not expected. Figure 4.3 C was acquired with a long TR and TE_{eff}. It is therefore expected to show T_2-weighting, i.e. bright vitreous, medium bright lipid, and a dark lens. The contrast in this image meets the expectations. Furthermore, the sclera is visible as a black line

between the vitreous and the lipid behind the eye. The maximum intensity in Figure 4.3 C is lower than in Figure 4.3 B. This is caused by the longer echo train used to obtain a T_2-weighted image, which results in an overall lower signal intensity. As a result, the SNR in this image is lower; this is clearly visible in Figure D.2 C.

Figure 4.3 D and E were acquired at a higher resolution (0.67 × 0.67 mm in-plane). The timings are equal to those of Figure 4.3 B and C, except for the TE of image D, which is increased to 12 ms; this increase was necessary due to the increased resolution. The contrast of these images is equal to the contrast in Figure 4.3 B and C. Due to the higher resolution, the SNR of these images is lower, which corresponds to the expectations. However, the visibility of some details improves, especially in the T_1-weighted scan (Figure 4.3 D): the eye wall can now clearly be distinguished from the surrounding lipid, and a structure around the lens is visible. Because this structure has the same intensity as the eye wall, it is probably the ciliary body. The same structure can also be distinguished on the lower resolution zero-filled scan in Figure D.1 B.

The last image in Figure 4.3 was acquired with a GRE readout, with timings similar to the timings used in TSE 4 (Figure 4.3 D). Compared with this image, Figure 4.3 F has a significantly lower SNR, and the eye wall cannot be distinguished from the lipid. Some details visible in Figure 4.3 D, for example the ciliary body, are not visible in this image. Furthermore, the intensities of the lipid and the lens are almost the same, but this could be caused by the shorter TR used in the GRE sequence.

5 Discussion

The results in Chapter 4 show that the eye coil works, and that it can be used to image porcine eyes at a resolution that allows to distinguish the most important structures in the eye. In this chapter, various aspects of the experiments and their possible implications for the interpretation of the results are discussed. Furthermore, the results are used to assess whether the design requirements have been met.

5.1. Technical aspects

5.1.1. Coupling changes

The coupling was found to have changed during the scans, which resulted in an increased reflection for both coils. A reflection of -20 dB means that 1% of the power transferred to the coil is reflected, i.e. 99% of the power is still transferred to the spectrometer. This means that the signal strength did not significantly change due to the increased coupling, so the SNR was not significantly affected by this change.

Unfortunately, it is unknown when exactly the coupling changed, and what caused this change. This is a reason to measure the coupling more often during future measurements. During the experiments, the positions of the phantom and the coils were not changed, and the setup was not touched. The coil positions may have been changed a bit by vibrations in the gradients. The setup is known to be very sensitive to small changes in the position of the eye coil, and even touching the coil may cause the coupling to increase considerably. In a clinical context, this would not be acceptable, because the coil will be positioned on the patient's head and therefore cannot be positioned very accurately. Furthermore, small movements by the patient could already result in strong coupling between the receive coil and the transmit coil. For clinical applications, it is therefore necessary to include a detuning circuit, which is currently not available on the low field system.

5.1.2. Penetration depth and FOV

The half-value depth $d_{1/2}$ determined in Section 4.1.2 does not characterise the penetration; it characterises signal decay. This allows for comparison of values obtained for different scans, since this method is relatively insensitive to differences between the sequences, whereas methods that depend on e.g. the SNR do depend on the sequence. From the results can therefore be concluded that the signal of the final eye coil prototype decays slower than that of the first prototype. However, the signal profile in Figure 4.2 shows that close to the coil the signal does not decay exponentially as a function of depth. This means that $d_{1/2}$ does not fully characterise the penetration depth. Furthermore, the penetration depth does not characterise the FOV of the coil; it does not say anything about the width of the FOV. From Figure 4.2 can be concluded that the FOV of the eye coil is large enough to contain an eye with a diameter of 25 mm, and also a part of the orbit.

It is also interesting that the images in Figures 4.3 and D.2 do not show a clear decrease in signal intensity along the axis of the eye. This could be caused by the position of the porcine eye with respect to the coil: the images in Figure 4.2 also show a relatively constant signal intensity at the position of the eye. To be sure about this, a reference scan of a porcine eye could be made using a volume coil, and compared with a scan made with the eye coil.

The reliability of the penetration depth values is limited by the optimal position of the eye coil. To reduce the inductive coupling between the transmit coil and the eye coil, the eye coil was positioned in a horizontal plane. As a result, the magnetic field of the coil was oriented perpendicular to B_0. In a clinical setting, the coil is likely to be tilted due to its position on the face of the patient. This will increase the component of the coil field parallel to B_0, and thus decrease the received signal. The effective FOV of the eye coil may therefore be smaller in a clinical setting. This is not necessarily a problem, because the current FOV is relatively large.

5.2. Imaging

The eye can clearly be distinguished in all images in Figure 4.3, which is an improvement over the first coil prototype. The CNR in image Figure 4.3 A is unacceptably low, making it difficult to distinguish the different tissues in the eye. The SNR in the other TSE images (Figure 4.3 B-D, TSE 2- 5) is better, due to the increased number of averages and slice thickness. In all these images, the SNR and in-plane resolution are high enough to distinguish the lens, vitreous, lipid and sclera or eye wall. The in-plane resolution of images D and E (0.67 × 0.67 mm) is even higher than the resolution used in the clinical protocol (0.8 × 0.8 mm) [1]. These images are noisy, but the SNR is still acceptable, because all relevant structures are visible.

The GRE image in Figure 4.3 F was acquired in about half the time needed for TSE scans at the same resolution, and has a much lower SNR. In order to get a higher SNR, more averages should be acquired, which will increase the acquisition time to values similar to the scan times of TSE scans. The contrast can possibly be improved by trying different values of TR and TE. However, based on the above arguments GRE sequences are not likely to outperform TSE sequences in terms of SNR and acquisition times.

The contrast in the images in Figure 4.3 is similar to the contrast in images acquired with the clinical protocol (Figure 1.1), with a few exceptions. On both field strengths, the T_2-weighted images show a bright vitreous, a dark lens and sclera, and lipid with medium brightness. The T_1-weighted images show a dark vitreous and bright lipid. The inner layers of the eye wall (choroid and retina) have a medium intensity. The most notable difference is found in the lens, which is relatively bright on the T_1-weighted low field images. This could indicate that the T_1 of the lens is lower at a low field strength, which corresponds with the notion that T_1 tends to decrease for a decreasing field strength [20]. Furthermore, the sclera is hardly visible in the T_1-weighted low field images, but it is visible in the clinical images. In the zero-filled images (Figure D.1) a thin black layer seems to be present at the back of the eye, but not as clear as in the clinical images. A possible explanation could be that partial voluming, caused by the high slice thickness, causes the sclera to be hidden by the choroid or retina. Finally, the lipid behind the eye is hypointense to the vitreous in the T_2-weighted images, whereas the intensities of both tissues are similar in the clinical images (Figure 1.1). This difference can be attributed to differences in T_2-weighting between the sequences used on the clinical and low field scanners. The clinical protocol has been optimised for tumour contrast, which is not the case for the sequences used on the low field scanner. Furthermore, the window/level settings of the MRI scan in Figure 1.1 are optimised for the tumour contrast, and may therefore not reliably reflect the intensity of tissues with a high intensity.

5.3. Fulfilment of the design requirements

Although there are some small anatomical differences between porcine and human eyes, the most important structures have a similar composition and size [31]. The images of porcine eyes can therefore be used to assess whether the setup used during the experiments meets the requirements listed in Section 1.2.

5.3.1. Field of View

As discussed in the Section 5.1.2, the FOV of the coil is large enough to contain the eye and orbit.

5.3.2. Contrast

A limitation of the experiments is that no eyes with tumours were scanned, so there is no data about the contrast of tumours at low field strength. However, given the similarities in contrast between high and low field images, tumours are likely to exhibit similar behaviour as well. In this case, tumours would have a high intensity on T_1-weighted images, and low to medium intensity on T_2-weighted images. On both weightings, the tumour can then be easily distinguished from the vitreous. On T_2-weighted images, the tumour could also be distinguished from the sclera, which is clearly visible on these images. The bad visibility of the sclera on T_1-weighted images could pose a problem for the contrast between the tumour and the back of the eye. It cannot be ruled out that the intensity of the tumour is similar to the intensity of the eye wall or the lipid surrounding the eye; in this case the contrast between tumour and eye wall may be poor, and T_1-weighted images need to be combined with T_2-weighted images for proper delineation of the tumour.

5.3.3. Resolution, scan time and SNR

Although the resolutions of TSE 2 – 5 were high enough to distinguish the most important structures in the eye, these resolutions could only be attained by using a low resolution in the slice direction. Slices of 7.5 mm were used, which is more than a quarter of the eye diameter. With this slice thickness, the images cannot be considered three-dimensional. However, this slice thickness was necessary to obtain images with a sufficiently high SNR in a decent amount of time. Increasing the resolution to the minimum required value of 1 mm isotropic would not only increase the scan time with a factor 7.5, but also decrease the SNR.

Suppose that the SNR of TSE 5 (Figure 4.3 E) is the minimum acceptable SNR. This result is already quite noisy, but most structures can still be distinguished. The resolution of this scan is changed to 1.0 mm isotropic; this decreases the in-plane resolution, but increases the resolution in the slice direction. The voxel size then decreases with a factor $3/2 \times 3/2 \times 1/7.5 = 0.3$. This approximately halves the SNR. Moreover, the number of k-space points changes as well, increasing the scan time with a factor $60/90 \times 60/8 = 5$. The scan time then becomes 00:35:10, which is about 9 times the required 4 minutes. The scan time can be reduced to a more acceptable value by reducing the number of averages. Since the original number of averages is 8, an additional reduction of the FOV is necessary to reduce the scan time by a factor of 9. Using the relations mentioned in Section 2.2, this reduction in scan time and FOV is found to reduce the SNR by about a factor of 0.3. In total, this means $\frac{\sqrt{9}}{\sqrt{0.3}} \approx 5.5$ times the SNR is needed in order to meet the requirements on scan time and resolution, while maintaining the SNR found in the results. This is close to the initial estimated SNR deficiency of a factor of 5 (1.2), but it should be noted that the accuracy of this original estimate is limited by the underlying assumptions.

Based on the above arguments, it can be concluded that the setup used during the experiments does not meet the design requirements. The system is limited by the lower SNR inherent to low field MRI, making it difficult to perform fast, high-resolution imaging in a small FOV. A scan that meets the minimum requirements will have a low SNR and CNR; as a reference, the SNR is expected to be lower than the SNR in Figure 4.3 A. In a clinical context, this means that the images are unusable, because the noise will obscure small structures and tissue boundaries. This results, for example, in unreliable tumour measurements. Scanning slightly longer than 4 minutes will not substantially improve the CNR, but is likely to result in motion artefacts. Substantially decreasing the resolution in one direction will essentially result in two-dimensional imaging. Moreover, reducing the resolution will reduce the reliability of tumour measurements. The currently achievable image quality can therefore not compete with ultrasound. However, if the system can be improved to deliver images of the same quality at a higher resolution, they would have clinical value and improve over the current standards.

5.4. Next steps

The previous section demonstrated that the SNR needs to be increased by more than a factor of 5, without adjusting imaging parameters like resolution. It is highly unlikely that optimising the pulse sequences, i.e. optimising the flip angle patterns and echo train lengths, will increase the SNR to the desired level. Furthermore, undersampling methods like half-Fourier acquisitions will reduce scan times, but also further decrease the SNR and can therefore not be used. In this section, a few other options to increase the SNR will be explored.

Although improving the eye coil design in order to increase the SNR seems an obvious option, the quality factor Q needs to be increased by about a factor of 30 for the required gain in SNR. This gain in Q is unrealistically high, given the already relatively high Q for the current design. Furthermore, replacing the surface coil with a volume coil is not feasible, because this will significantly increase the required FOV and scan times.

Increasing the static magnetic field strength is a more realistic option. At low field strengths, the SNR is proportional to $B_0^{3/2}$ [20]. This means that a three times stronger static field, i.e. $B_0 \approx 150$mT, would sufficiently improve the SNR. A stronger field requires a different magnet, and further research is needed to determine if this field strength can still be accomplished with a Halbach array.

Other reconstruction methods can also be used to improve the SNR of the images. Regularised [32] and deep learning based [33, 34] reconstruction methods have been developed for low field MRI, and were shown to increase the SNR with respect to conventional reconstruction methods. However, denoising images with a very low SNR is likely to result in the loss of details like the sclera and small tumours. Furthermore, deep learning based methods generally need large amounts of training data. These data are readily available for some anatomies, but not for the eye.

Finally, the SNR is likely to improve as a result of further developments of the low field scanner. Improved RF amplifier designs and RF shielding may reduce noise, and adding a preamplifier close to the coil will reduce signal losses in the transmission line. In combination with the aforementioned options, these improvements could increase the SNR sufficiently to meet the design requirements. In that case, additional research is needed to develop a clinically useable system. First, the tumour contrast needs to be determined by ex-vivo scanning of enucleated eyes. In-vivo experiments on healthy and diseased volunteers should be performed, which requires the development of a detuning circuit to prevent the observed problems with inductive coupling. Pulse sequences should be further optimised, in order to optimise contrast for the tumour and minimise scan times. Lastly, it is necessary to develop a contrast-enhanced sequence, which enhances the visibility of UM, further increases the SNR, and allows for the diagnosis of retinal detachment.

6

Conclusion

It is possible to image the eye using the current low field MRI scanner, but the design requirements are not met. The field of view of the eye coil is sufficient to image the eye and the orbit. The vitreous body, lens, lipid and sclera can be distinguished in images of porcine eyes, and the contrast is similar to the contrast seen in clinical images. However, the resolution of the images is lower than 1.0 mm isotropic, and the acquisition time exceeds 4 minutes. Increasing the resolution and decreasing the scan time will significantly reduce the SNR, which degrades image quality and reduces the ability to distinguish between tissues. Fast, high-resolution imaging is therefore not possible with the current setup. The SNR can be increased by using a stronger static magnetic field, which requires the development of new hardware. If a higher SNR can be realised, it is necessary to determine tumour contrast, design optimised pulse sequences, and test the method on human subjects, in order to develop a clinically useable system.

References

[1] Teresa Ferreira et al. "MRI of Uveal Melanoma". In: *Cancers* 11.3 (Mar. 17, 2019), p. 377. ISSN: 2072-6694. DOI: 10.3390/cancers11030377. URL: https://www.mdpi.com/2072-6694/11/3/377 (visited on 11/15/2021).

[2] Pietro Valerio Foti et al. "Diagnostic Methods and Therapeutic Options of Uveal Melanoma with Emphasis on MR Imaging—Part I: MR Imaging with Pathologic Correlation and Technical Considerations". In: *Insights Imaging* 12.1 (Dec. 2021), p. 66. ISSN: 1869-4101. DOI: 10.1186/s13244-021-01000-x. URL: https://insightsimaging.springeropen.com/articles/10.1186/s13244-021-01000-x (visited on 11/15/2021).

[3] Myriam G. Jaarsma-Coes et al. "Comparison of Magnetic Resonance Imaging–Based and Conventional Measurements for Proton Beam Therapy of Uveal Melanoma". In: *Ophthalmology Retina* (July 13, 2022). ISSN: 2468-6530. DOI: 10.1016/j.oret.2022.06.019. URL: https://www.sciencedirect.com/science/article/pii/S2468653022003396 (visited on 09/12/2022).

[4] Jan-Willem M. Beenakker et al. "Clinical Evaluation of Ultra-High-Field MRI for Three-Dimensional Visualisation of Tumour Size in Uveal Melanoma Patients, with Direct Relevance to Treatment Planning". In: *Magn Reson Mater Phy* 29.3 (June 2016), pp. 571–577. ISSN: 0968-5243, 1352-8661. DOI: 10.1007/s10334-016-0529-4. URL: http://link.springer.com/10.1007/s10334-016-0529-4 (visited on 11/15/2021).

[5] Myriam G. Jaarsma-Coes et al. "MRI Enables Accurate Diagnosis and Follow-up in Uveal Melanoma Patients after Vitrectomy". In: *Melanoma Research* 29.6 (Dec. 2019), pp. 655–659. ISSN: 0960-8931. DOI: 10.1097/CMR.0000000000000568. URL: https://journals.lww.com/melanomaresearch/Fulltext/2019/12000/MRI_enables_accurate_diagnosis_and_follow_up_in.13.aspx (visited on 06/21/2022).

[6] Laurel B. Tanke, David A. Leske, and Lauren A. Dalvin. "Conversion Factor for B-Scan Ultrasound Measurement of Intraocular Tumors With and Without the Sclera". In: *Journal of Ultrasound in Medicine* 40.9 (2021), pp. 1911–1917. ISSN: 1550-9613. DOI: varia. URL: https://onlinelibrary.wiley.com/doi/abs/10.1002/jum.15575 (visited on 09/08/2022).

[7] Tommaso Tartaglione et al. "Uveal Melanoma: Evaluation of Extrascleral Extension Using Thin-Section MR of the Eye with Surface Coils". In: *Radiol med* 119.10 (Oct. 1, 2014), pp. 775–783. ISSN: 1826-6983. DOI: 10.1007/s11547-014-0388-x. URL: https://doi.org/10.1007/s11547-014-0388-x (visited on 11/10/2022).

[8] Teresa A. Ferreira et al. "MR Imaging Characteristics of Uveal Melanoma with Histopathological Validation". In: *Neuroradiology* 64.1 (Jan. 1, 2022), pp. 171–184. ISSN: 1432-1920. DOI: 10.1007/s00234-021-02825-5. URL: https://doi.org/10.1007/s00234-021-02825-5 (visited on 10/14/2022).

[9] Bart de Vos et al. "Design, Characterisation and Performance of an Improved Portable and Sustainable Low-Field MRI System". In: *Front. Phys.* 9 (July 26, 2021), p. 701157. ISSN: 2296-424X. DOI: 10.3389/fphy.2021.701157. URL: https://www.frontiersin.org/articles/10.3389/fphy.2021.701157/full (visited on 12/09/2021).

[10] D. H. Char et al. "Ultrasonographic Measurement of Uveal Melanoma Thickness: Interobserver Variability." In: *British Journal of Ophthalmology* 74.3 (Mar. 1, 1990), pp. 183–185. ISSN: 0007-1161, 1468-2079. DOI: 10.1136/bjo.74.3.183. pmid: 2182105. URL: http://bjo.bmj.com/content/74/3/183 (visited on 09/14/2022).

[11] *Vitreous Body*. In: *Wikipedia*. June 2, 2022. URL: https://en.wikipedia.org/w/index.php?title=Vitreous_body&oldid=1091062399 (visited on 09/08/2022).

[12] Lisa Klaassen et al. "Automatic Three-Dimensional Magnetic Resonance-based Measurements of Tumour Prominence and Basal Diameter for Treatment Planning of Uveal Melanoma". In: *Physics and Imaging in Radiation Oncology* 0.0 (Nov. 6, 2022). ISSN: 2405-6316. DOI: 10.1016/j.phro.2022.11.001. URL: https://phiro.science/article/S2405-6316(22)00091-4/fulltext (visited on 11/08/2022).

[13] Inessa Bekerman, Paul Gottlieb, and Michael Vaiman. "Variations in Eyeball Diameters of the Healthy Adults". In: *J Ophthalmol* 2014 (2014), p. 503645. ISSN: 2090-004X. DOI: 10.1155/2014/503645. pmid: 25431659. URL: https://www.ncbi.nlm.nih.gov/pmc/articles/PMC4238270/ (visited on 09/05/2022).

[14] Elaine Nicpon Marieb and Katja Hoehn. *Human Anatomy & Physiology*. Eleventh edition, global edition. Harlow: Pearson, 2019. 1266 pp. ISBN: 978-1-292-26085-3 978-1-292-26103-4.

[15] Mahmood F. Mafee et al. "Anatomy and Pathology of the Eye: Role of MR Imaging and CT". In: *Neuroimaging Clinics of North America*. Ophthalmologic Neuroimaging 15.1 (Feb. 1, 2005), pp. 23–47. ISSN: 1052-5149. DOI: 10.1016/j.nic.2005.02.005. URL: https://www.sciencedirect.com/science/article/pii/S1052514905000067 (visited on 09/06/2022).

[16] Thomas O'Reilly and Andrew G. Webb. "In Vivo T1 and T2 Relaxation Time Maps of Brain Tissue, Skeletal Muscle, and Lipid Measured in Healthy Volunteers at 50 mT". In: *Magnetic Resonance in Medicine* 87.2 (2022), pp. 884–895. ISSN: 1522-2594. DOI: 10.1002/mrm.29009. URL: https://onlinelibrary.wiley.com/doi/abs/10.1002/mrm.29009 (visited on 05/02/2022).

[17] C Haasjes. "Ultrasound Imaging in Ocular Oncology: A Systematic Review". Unpublished literature study. 2022.

[18] C Haritoglou. "Interobserver and Intraobserver Variability of Measurements of Uveal Melanomas Using Standardised Echography". In: *British Journal of Ophthalmology* 86.12 (Dec. 1, 2002), pp. 1390–1394. ISSN: 00071161. DOI: 10.1136/bjo.86.12.1390. URL: https://bjo.bmj.com/lookup/doi/10.1136/bjo.86.12.1390 (visited on 06/10/2022).

[19] Daniel Kook et al. "Variability of Standardized Echographic Ultrasound Using 10 mHz and High-Resolution 20 mHz B Scan in Measuring Intraocular Melanoma". In: *OPTH* 5 (Apr. 18, 2011), pp. 477–482. DOI: 10.2147/OPTH.S18513. URL: https://www.dovepress.com/variability-of-standardized-echographic-ultrasound-using-10-mhz-and-hi-peer-reviewed-fulltext-article-OPTH (visited on 09/08/2022).

[20] José P. Marques, Frank F.J. Simonis, and Andrew G. Webb. "Low-Field MRI: An MR Physics Perspective". In: *Journal of Magnetic Resonance Imaging* 49.6 (2019), pp. 1528–1542. ISSN: 1522-2586. DOI: 10.1002/jmri.26637. URL: https://onlinelibrary.wiley.com/doi/abs/10.1002/jmri.26637 (visited on 12/16/2021).

[21] Thomas O'Reilly et al. "In Vivo 3D Brain and Extremity MRI at 50 mT Using a Permanent Magnet Halbach Array". In: *Magn. Reson. Med.* 85.1 (Jan. 2021), pp. 495–505. ISSN: 0740-3194, 1522-2594. DOI: 10.1002/mrm.28396. URL: https://onlinelibrary.wiley.com/doi/10.1002/mrm.28396 (visited on 01/12/2022).

[22] Andrew Webb, ed. *Magnetic Resonance Technology: Hardware and System Component Design*. New Developments in NMR No. 7. Cambridge, UK: Royal Society of Chemistry, 2016. 385 pp. ISBN: 978-1-78262-359-5.

[23] Bernhard Gruber et al. "RF Coils: A Practical Guide for Nonphysicists: RF Coils". In: *J. Magn. Reson. Imaging* 48.3 (Sept. 2018), pp. 590–604. ISSN: 10531807. DOI: 10.1002/jmri.26187. URL: https://onlinelibrary.wiley.com/doi/10.1002/jmri.26187 (visited on 01/28/2022).

[24] Robert W. Brown, ed. *Magnetic Resonance Imaging: Physical Principles and Sequence Design*. 2. ed. Hoboken, NJ: Wiley Blackwell, 2014. 944 pp. ISBN: 978-0-471-72085-0.

[25] Olaf Dietrich et al. "Measurement of Signal-to-Noise Ratios in MR Images: Influence of Multichannel Coils, Parallel Imaging, and Reconstruction Filters". In: *Journal of Magnetic Resonance Imaging* 26.2 (2007), pp. 375–385. ISSN: 1522-2586. DOI: 10.1002/jmri.20969. URL: https://onlinelibrary.wiley.com/doi/abs/10.1002/jmri.20969 (visited on 05/10/2022).

[26] T. O'Reilly, W. M. Teeuwisse, and A. G. Webb. "Three-Dimensional MRI in a Homogenous 27 cm Diameter Bore Halbach Array Magnet". In: *Journal of Magnetic Resonance* 307 (Oct. 1, 2019), p. 106578. ISSN: 1090-7807. DOI: 10.1016/j.jmr.2019.106578. URL: https://www.sciencedirect.com/science/article/pii/S1090780719302174 (visited on 12/20/2021).

[27] Bart de Vos et al. "Gradient Coil Design and Realization for a Halbach-Based MRI System". In: *IEEE Trans. Magn.* 56.3 (Mar. 2020), pp. 1–8. ISSN: 0018-9464, 1941-0069. DOI: 10.1109/TMAG.2019.2958561. URL: https://ieeexplore.ieee.org/document/8961197/ (visited on 12/09/2021).

[28] Keysight. *U1733C 100Hz/120Hz/1kHz/10kHz/100kHz Handheld LCR Meter*. Keysight. URL: https://www.keysight.com/us/en/product/U1733C/handheld-lcr-meter-100-hz-120-hz-1-khz-10-khz100-khz.html (visited on 09/06/2022).

[29] *3M™ Fluorinert™ Electronic Liquid FC-3283*. URL: https://www.3m.com/3M/en_US/p/d/b00043108/ (visited on 10/13/2022).

[30] *Discontinued: S5048 2-Port 4.8 GHz Analyzer*. Copper Mountain Technologies. URL: https://coppermountaintech.com/discontinued-s5048-2-port-4-8-ghz-analyzer/ (visited on 11/07/2022).

[31] Sheldon Middleton. "Porcine Ophthalmology". In: *Veterinary Clinics of North America: Food Animal Practice* 26.3 (Nov. 2010), pp. 557–572. ISSN: 07490720. DOI: 10.1016/j.cvfa.2010.09.002. URL: https://linkinghub.elsevier.com/retrieve/pii/S074907201000040X (visited on 10/26/2022).

[32] Merel de Leeuw den Bouter, Martin van Gijzen, and Rob Remis. "Low-Field Magnetic Resonance Imaging Using Multiplicative Regularization". In: *Magnetic Resonance Imaging* 75 (Jan. 2021), pp. 21–33. ISSN: 0730725X. DOI: 10.1016/j.mri.2020.10.001. URL: https://linkinghub.elsevier.com/retrieve/pii/S0730725X20306068 (visited on 12/09/2021).

[33] Reina Ayde et al. "Deep Learning for Fast Low-Field MRI Acquisitions". In: *Sci Rep* 12.1 (1 July 6, 2022), p. 11394. ISSN: 2045-2322. DOI: 10.1038/s41598-022-14039-7. URL: https://www.nature.com/articles/s41598-022-14039-7 (visited on 10/27/2022).

[34] N. Koonjoo et al. "Boosting the Signal-to-Noise of Low-Field MRI with Deep Learning Image Reconstruction". In: *Sci Rep* 11.1 (1 Apr. 15, 2021), p. 8248. ISSN: 2045-2322. DOI: 10.1038/s41598-021-87482-7. URL: https://www.nature.com/articles/s41598-021-87482-7 (visited on 10/27/2022).

[35] Jeff Bezanson et al. "Julia: A Fresh Approach to Numerical Computing". In: *SIAM Rev.* 59.1 (Jan. 2017), pp. 65–98. ISSN: 0036-1445, 1095-7200. DOI: 10.1137/141000671. URL: https://epubs.siam.org/doi/10.1137/141000671 (visited on 11/07/2022).

[36] John P. Mugler III. "Optimized Three-Dimensional Fast-Spin-Echo MRI". In: *Journal of Magnetic Resonance Imaging* 39.4 (2014), pp. 745–767. ISSN: 1522-2586. DOI: 10.1002/jmri.24542. URL: https://onlinelibrary.wiley.com/doi/abs/10.1002/jmri.24542 (visited on 05/10/2022).

[37] Matt A. Bernstein, Kevin Franklin King, and Ziaohong Joe Zhou. *Handbook of MRI Pulse Sequences*. Amsterdam ; Boston: Academic Press, 2004. 1017 pp. ISBN: 978-0-12-092861-3.

[38] Matthias Weigel. "Extended Phase Graphs: Dephasing, RF Pulses, and Echoes - Pure and Simple". In: *Journal of Magnetic Resonance Imaging* 41.2 (2015), pp. 266–295. ISSN: 1522-2586. DOI: 10.1002/jmri.24619. URL: https://onlinelibrary.wiley.com/doi/abs/10.1002/jmri.24619 (visited on 03/15/2022).

[39] Julien Lamy. *Sycomore — an MRI Simulation Toolkit*. May 27, 2022. URL: https://github.com/lamyj/sycomore (visited on 07/07/2022).

[40] S. Meiboom and D. Gill. "Modified Spin-Echo Method for Measuring Nuclear Relaxation Times". In: *Review of Scientific Instruments* 29.8 (Aug. 1958), pp. 688–691. ISSN: 0034-6748. DOI: 10.1063/1.1716296. URL: https://aip.scitation.org/doi/abs/10.1063/1.1716296 (visited on 09/05/2022).

A

Preliminary Experiments

Many design decisions mentioned in Chapter 3 are based on experiments performed with an early coil prototype. This appendix gives an overview of the experiments that were relevant for later design decisions.

A.1. Coil design

A coil as schematically depicted in Figure 2.1 is constructed (Figure A.1). The coil consists of five loops of single-stranded copper wire with a diameter of 1.5 mm, and is attached to a plastic base plate, designed to position the coil anterior to the eye. Further details of the coil are provided in Table A.1. In this first iteration, an existing base plate is used and the choice of the coil dimensions is based on the space available on the base plate.

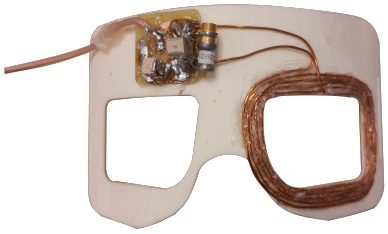

Figure A.1: Picture of the first eye coil prototype. The solid copper wire is glued to a curved, plastic base plate. The tuning and matching circuit is similar to the circuit shown in Figure 3.4.

Number of loops	5
Largest inner dimensions	50.4 × 30.8 mm
Largest outer dimensions	60.9 × 50.5 mm
C_T	2503 pF
C_M	245.3 pF
Q	70.6

Table A.1: Properties of the first eye coil. The quality factor has been measured outside the magnet.

A.2. Determination of the penetration depth

3D TSE scans of a water phantom are performed with different RF amplitudes, using only the eye coil. Because the transmit field of a surface coil is not homogeneous, the desired flip angle will only be reached at a single depth. Closer to the coil the flip angle will be larger, and further from the coil it will be smaller, in both cases resulting in a lower signal. Increasing the RF amplitude will increase the depth at which the desired flip angle is reached. Parameters for all scans are readout/phase 1/phase 2: z/y/x; FOV: 150 × 60 × 150 mm; resolution: 1.5 × 1.5 × 1.5 mm; $TR/TE/TE_{eff}$: 1000 ms/15 ms/15 ms (in-out k-space trajectory); echo train length: 30. Duration for each scan is 00:02:18. Transmit powers range from -21.50 dBm to 17.50 dBm, in steps of 1 dBm. The penetration depth is determined along the anterior - posterior axis, using the procedure explained in Section 3.4.1.

A.2.1. Results

Figure A.2 shows a signal profile and a slice of the image for each RF amplitude. In each profile, the signal first goes up, attains a maximum value, and then decays. This is caused by the inhomogeneous transmit field of the surface coil. As a result, the exponential fit cannot be performed on the full profile. Instead, only the decay section of the profile is used for the fit. Table A.2 lists the fit results and corresponding half value depths.

Setup	Transmit power [dBm]	Fit	$d_{1/2}$ [mm]
Combined Rx/Tx	-21.5	$5.32e^{-0.11y} + 0.06$	6.48 ± 0.86
Combined Rx/Tx	-20.5	$5.62e^{-0.10y} + 0.02$	6.96 ± 1.17
Combined Rx/Tx	-19.5	$12.77e^{-0.13y} + 0.06$	5.53 ± 0.87
Combined Rx/Tx	-18.5	$26.53e^{-0.15y} + 0.06$	4.69 ± 0.80
Combined Rx/Tx	-17.5	$5.33e^{-0.10y} + 0.02$	7.17 ± 1.59
Separate Rx/Tx	-18	$48.88e^{-0.05y} + 0.02$	13.89 ± 0.32

Table A.2: Fits and penetration depths for the eye coil using different setups and transmit powers. The top five rows are results obtained with the eye coil as receive and transmit coil. The bottom row is the result obtained using a separate transmit coil. Rx = receive, Tx = transmit.

A.3. Imaging using a separate transmit coil

A 3D TSE scan of a water phantom is performed using the eye coil as receive coil and a 200 mm solenoid coil (Section 3.1) as transmit coil. Because the transmit field of this coil is approximately homogeneous, only a single transmit power is used. Scan parameters are readout/phase 1/phase 2: z/y/x; FOV: 180 × 180 × 180 mm; resolution: 1.5 × 1.5 × 1.5 mm; $TR/TE/TE_{eff}$: 1000 ms/15 ms/15 ms (in-out k-space trajectory); echo train length: 30. Total scan duration is 00:08:08.

A.3.1. Results

Figure A.3 shows a signal profile from the center of the coil, and a slice from the image acquired using separate receive and transmit coils. The fit and penetration depth are included in Table A.2. The signal intensity halves over a distance of 14 mm, which is approximately half the diameter of a human eye. This penetration depth is nearly twice as large as the largest penetration depth found in Section A.2.1.

A.4. Imaging a porcine eye

Several images of a porcine eye are made, of which only the best results will be presented. Scan parameters are listed in Table A.3. Images are reconstructed without and with zero-filling and filtering performed on the k-space data.

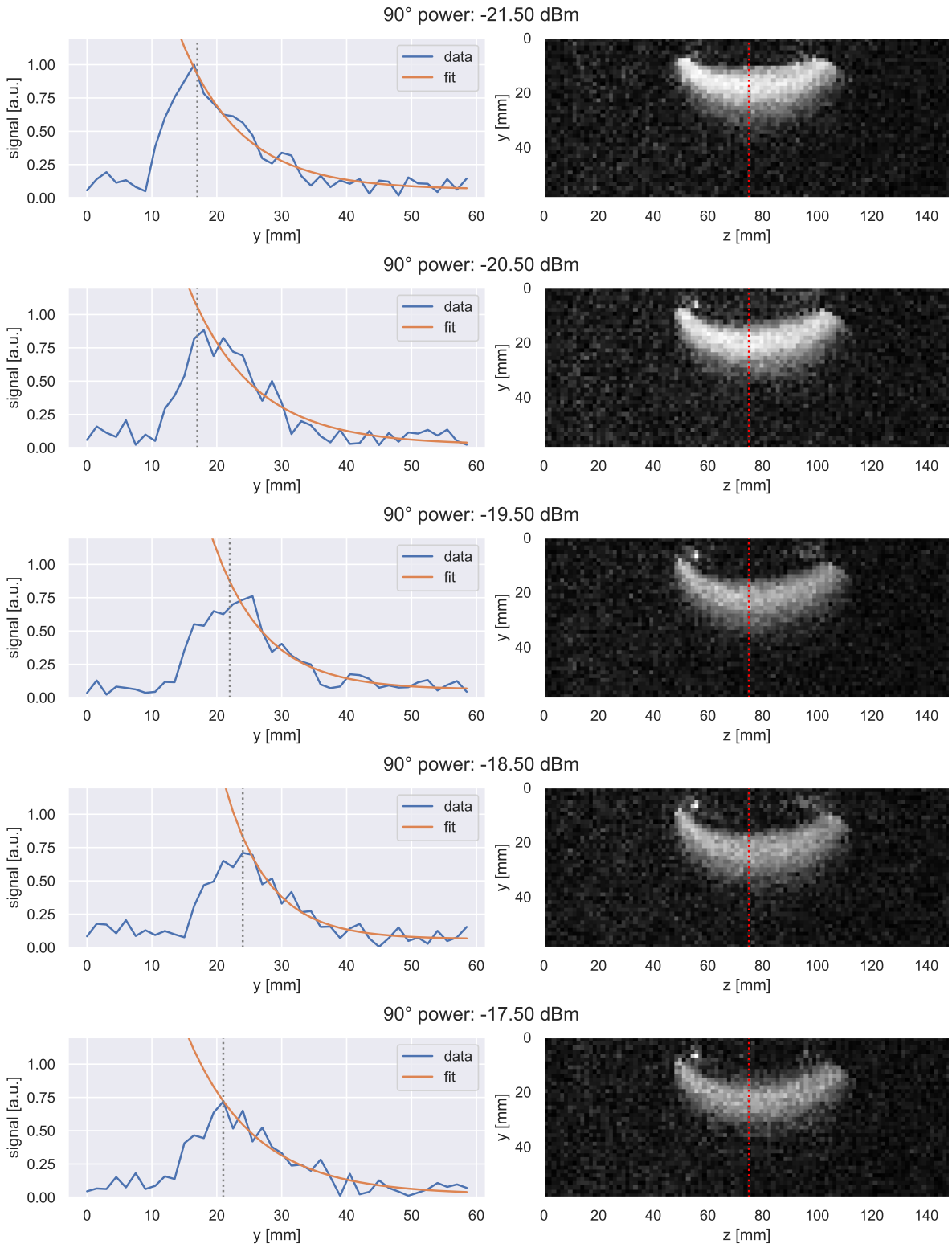

Figure A.2: Signal profiles (left column) obtained from images of a phantom (right column), acquired with different RF powers. The profiles have been normalised to the maximum value of all profiles. The transmit power for the excitation pulse (90°) is indicated above each row. The dotted vertical line in each profile indicates the left boundary of the region in which the fit is performed. The red, dotted lines in the images indicate the location of the profile. The phantom is circular, but the images show no signal originating from the top of the phantom. This is partly caused by a bubble, but also by the transmit field: close to the coil, the flip angle is close to 180°, resulting in a weak signal.

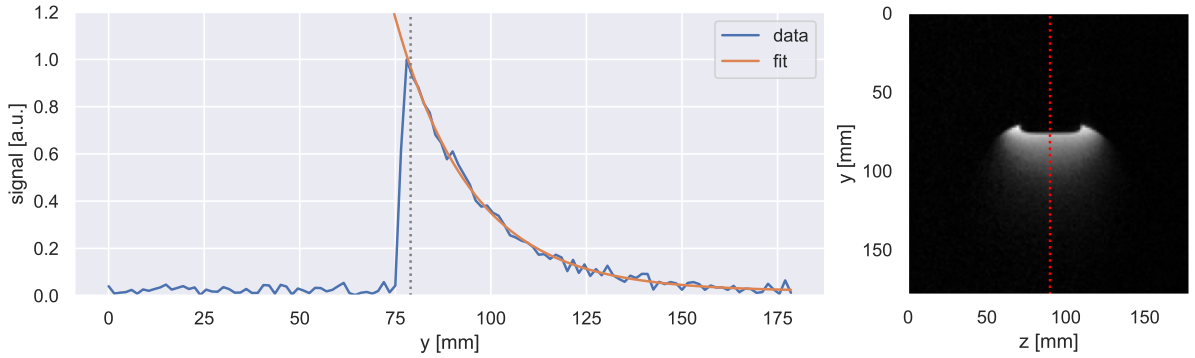

Figure A.3: Signal profile (left diagram) obtained from an image of a phantom (right diagram). The profile is normalised to its maximum value. The dotted vertical line in the profile indicates the left boundary of the region in which the fit is performed. The red, dotted line in the image indicates the location of the profile.

	Weighting	FOV [mm]	Resolution [mm]	Averages	$TR/TE/TE_{eff}$ [ms]	ETL	Trajectory	Duration [mm:ss]
TSE 1	T_2	80 × 40 × 80	1.25 × 2.5 × 2.5	4	2000/9/72	16	linear	04:16
TSE 2	T_1	80 × 40 × 80	1.25 × 2.5 × 2.5	8	200/9/9	4	in-out	03:28
TSE 3	T_1	40 × 40 × 60	0.63 × 1.67 × 1.88	8	200/9/9	4	in-out	05:12

Table A.3: Scan parameters and durations for various scans of a porcine eye. The readout/phase 1/phase 2 directions are z/y/x.

A.4.1. Results

All results are noisy, and the eye is hardly visible without postprocessing. After zero-filling and applying a squared sine bell filter on k-space, the lens and vitreous can be discovered in the images from TSE 1 and TSE 2. The contrast is as expected: a dark lens and bright vitreous for the T_2-weighted TSE 1, and a bright lens and dark vitreous for the T_1-weighted TSE 2. The sclera cannot be discerned in both scans, which can indicate that the resolution is too low. The result of TSE 3 has a significantly lower SNR, which is expected for images with a smaller FOV and higher resolution. Without processing, the eye is not visible; after filtering and zero-filling, the eye is still hardly visible. With a higher filter strength (Figure A.5), the largest structures in the eye can be distinguished, but the image quality is unacceptably low. The bad performance in this case could also be caused by the higher gradient strength needed for the smaller FOV. The gradients in the low field system may not perform well at very high strengths. In any case, the low SNR signifies that a larger FOV should be used, which means that gradient performance is not likely to be a limiting factor for the final result.

Except for TSE 2, all scans took longer than 4 minutes, which is longer than the limit set in Section 1.2. The acquisition time for TSE 2 is also close to this limit. Obtaining images with a higher SNR with this setup would for all cases result in scan times that exceed 4 minutes. These results therefore demonstrate that the current coil does not meet the design requirements.

A.5. Conclusion

In conclusion, the results show that the use of a separate transmit and receive coil significantly improves the penetration depth. The final prototype will therefore use this two-coil setup. Furthermore, a small FOV is not feasible, due to the low SNR of the images and presumed problems with gradient performance. In the final prototype, a higher SNR can be obtained in two ways. First, acquiring a larger FOV increases the SNR, which also allows for a larger coil with a larger penetration depth. Second, a higher quality factor

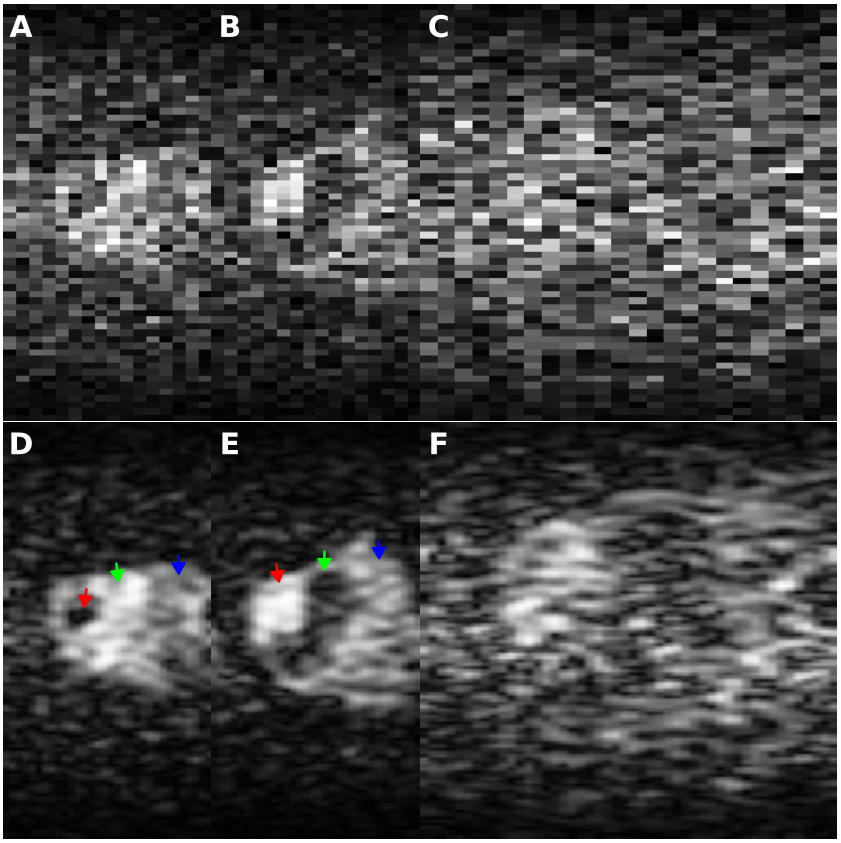

Figure A.4: Slices from the results of three TSE scans, reconstructed from unprocessed k-space data (top row, **A**-**C**) and zero-filled and filtered data (bottom row, **D**-**F**). Images **A**-**C** are from scans 1, 2 and 3 respectively. The eye is hardly visible in the unprocessed images; only in **B** it is possible to recognise the lens and the vitreous. After zero-filling and filtering (filter strength = 0.5), the results improve a bit, and the lens (red arrow), vitreous (green arrow) and lipid (blue arrow) can be distinguished. The results of TSE 3 are bad in both cases.

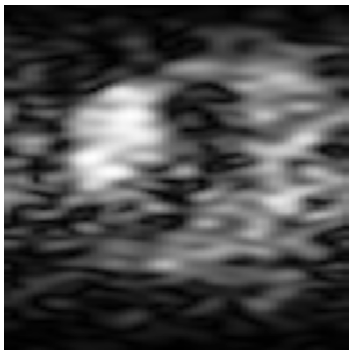

Figure A.5: Slice of TSE 3 from the preliminary experiments (Section A.4), zero-filled and filtered with a filter strength of 1.0. The lens, vitreous and lipid behind the eye are now visible, but the image shows strong blurring and its quality is still very low.

(Q) will increase the SNR. The final prototype will therefore be larger than the current prototype, and its Q will be improved by using Litz wire instead of single-stranded copper wire.

B

Magnetic Field Simulations

Based on the results obtained with the first coil (Appendix A), a new coil was designed. The dimensions of this coil were based on magnetic field simulations using the Biot-Savart law:

$$\mathbf{B}(\mathbf{r}) = \frac{\mu_0}{4\pi} \int_C \frac{I d\,\ell \times \mathbf{r}'}{|\mathbf{r}'|^3}. \tag{B.1}$$

This equation expresses the magnetic field **B** at a point in space **r** as an integral over the path C, which is in this case the RF coil. I is the current flowing through the coil, ℓ is a point on the path C, $d\ell$ is a tangent vector of C in the point ℓ, and $\mathbf{r}' = \mathbf{r} - \ell$.

The simulations were implemented in Julia 1.8.2 [35] and are available at `https://git.lumc.nl/chaasjes/CoilSimulations.jl`. In these simulations, the coil was modelled as a single rectangular wire wrapped around a cylinder with a radius R of 13 cm, and parametrised with a height h (the length of the straight legs) and a width w (the distance between the straight legs). The model and the coordinate system used in the simulations are visualised in Figure B.1. The coordinate system is not related to the scanner coordinate system. In these simulations, all constants in (B.1) are ignored.

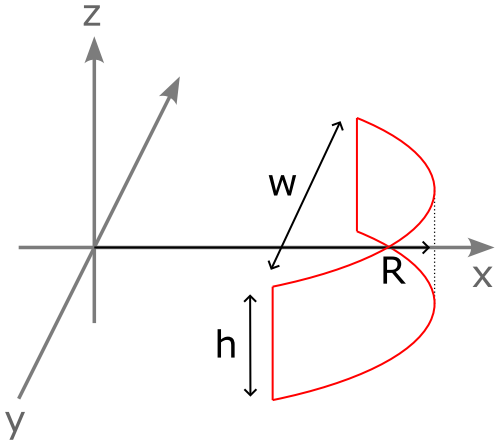

Figure B.1: Model of the coil used for the simulations. The coil consists of a single square loop (depicted in red), wrapped around a cylinder with radius R. The coil height h indicates the length of the straight legs of the coils, and the width w indicates the distance between the straight legs.

The results of the simulations for several coil sizes are shown in Figure B.2 and B.3. The profiles in Figure B.2 show that all simulated coils differ significantly from the old coil, but the differences between the other coils are small. Wider coils result in a lower signal close to the coil, because the straight legs move further away from the coil center, thus reducing their contribution to the magnetic field in the center of

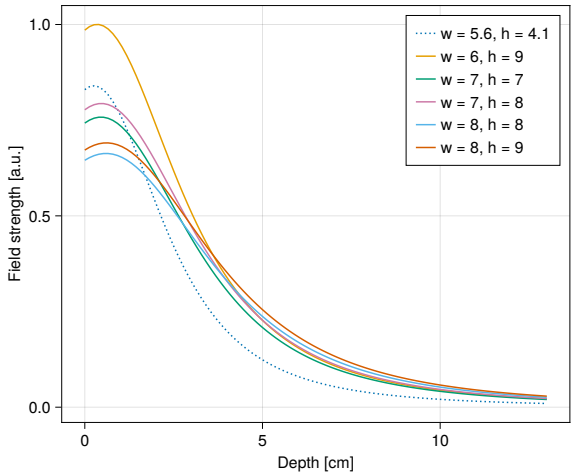

Figure B.2: Center profiles of the simulated field along x ($y = z = 0$), for coils of different sizes. The coil center is located at a depth of 0 cm. The dotted line ($w = 5.6, h = 4.1$) corresponds to the center loop of the first coil prototype, used in Appendix A. All sizes are in centimetres.

the coil. The same effect is also observed when the height is increased, but it is much smaller. This can be explained by the fact that increasing the width also causes the straight legs to move away from the center in the x-direction.

The use of these simulations is limited: the coil geometry is different, the simulated coil consists of only a single loop, and only the static field is simulated. Furthermore, the effect of the B_0 field of the scanner is not incorporated in the simulations. When a loop coil is positioned perpendicular to B_0, the penetration depth decreases. Increasing the width of the coil may ultimately increase its size in a plane perpendicular to B_0, in which case the simulated increase in penetration is an overestimation. When imaging a patient, this can become a problem, because the coil will then be located on one side of the head, and B_0 points in the left - right direction. What can be concluded from these simulations, is that a larger coil is able to significantly increase the penetration depth. However, this effect is smaller when using larger coils. For example, using a coil of 8 × 8 cm instead of the old 5.6 × 4.1 cm will significantly improve the FOV, but this difference is rather small with respect to a 7 × 7 cm coil.

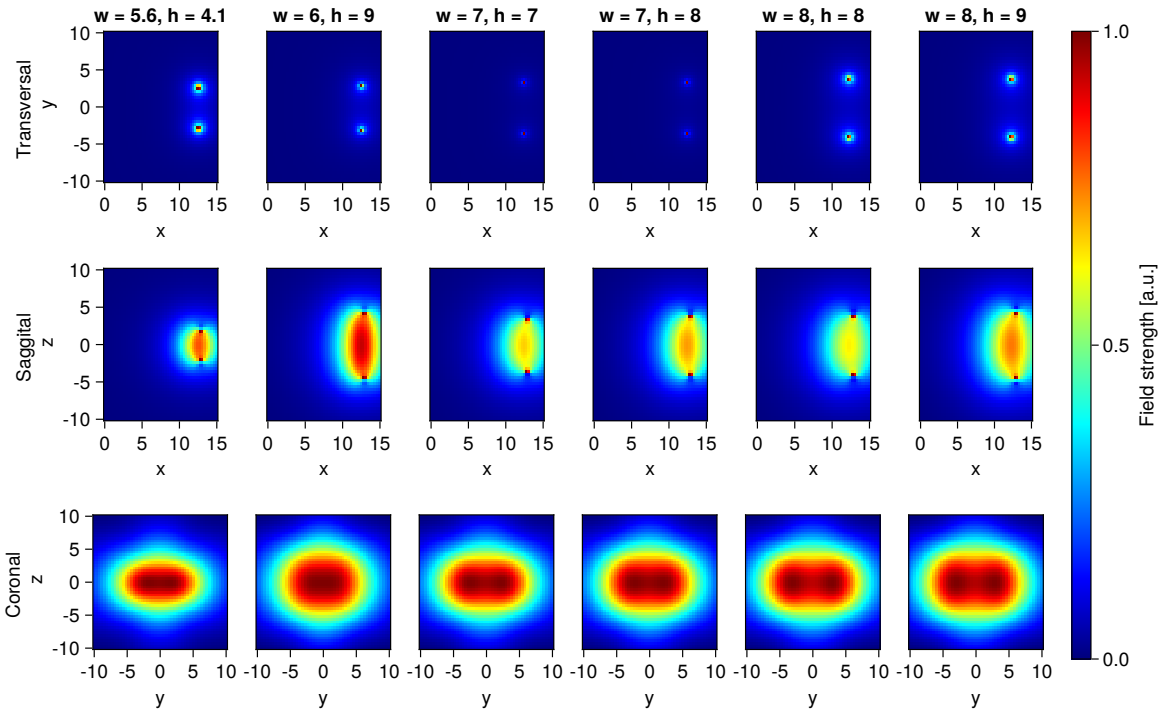

Figure B.3: Transversal (*xy*-plane), sagittal (*xz*-plane) and coronal (*yz*-plane) field maps of the simulated field for coils of different sizes. The first column corresponds to the center loop of the first coil prototype. All sizes are in centimetres. The coronal slices are located at a depth of 5 cm below the coil, which is a rough estimate of the location of the back of the eye.

C

Simulation of TSE sequences with EPG

MRI is an inherently slow imaging modality, but imaging the eye requires a fast imaging protocol. Although some time can be saved by limiting the field of view (FOV), this is generally not enough. Moreover, decreasing the FOV also results in a lower SNR. The acquisition time can also be decreased by using a fast pulse sequence. There is a large number of fast sequences available, which can be roughly divided into two categories: fast gradient echo (or fast field echo, FFE) and Fast Spin Echo (FSE; also known as Turbo Spin Echo, TSE). This appendix will focus on TSE, since attempts to image porcine eyes with gradient echo sequences did not yield satisfactory results.

It is possible to use a very basic TSE sequence for imaging the eye, but this does generally not result in optimal images. Optimizing the sequence for the relaxation times encountered in the eye can yield images with a better contrast, and further improve scan times. Signal simulations play an important role in the design of an eye-specific sequence. The following sections explain the key parameters of a TSE sequence and the simulation method used to design a better sequence.

C.1. Turbo Spin Echo

A TSE sequence is a spin echo (SE) sequence with multiple echoes. As in a SE sequence, the sequence starts with an excitation pulse, tipping the longitudinal magnetization M_z into the transverse plane. The transverse magnetization $M_\perp$ experiences exponential decay, which is caused by two processes. The first process are spin-spin interactions; this decay is characterized by the transverse relaxation time T_2. The second process is dephasing due to inhomogeneities in the static B_0 field; this decay can be characterized using a different relaxation time, T_2'. Together, these processes result in an effective relaxation time T_2^*, defined as $1/T_2^* = 1/T_2 + 1/T_2'$.

Spin echo exploits the fact that the signal decay due to magnetic field inhomogeneities can be reversed. By applying a refocusing pulse, the orientations of the spins are reversed, and they will rephase again. This causes the transverse magnetization to increase, ultimately leading to a local maximum called the 'echo'. If the refocusing pulse is applied at a time $t = \tau$, the echo will occur at the echo time $TE = 2\tau$. At this moment, the spins are in phase; afterwards, they will dephase again. During this process, a single line of k-space is acquired, in which the center of the line is acquired at TE. In a normal SE sequence, the sequence ends here, and this process is repeated for every line in k-space. A significant delay is added between the repetitions, to allow for further decay of $M_\perp$ and sufficient regrowth of M_z. TSE goes a step further, and applies multiple refocusing pulses during each repetition. At each echo, a separate line of k-space is ac-

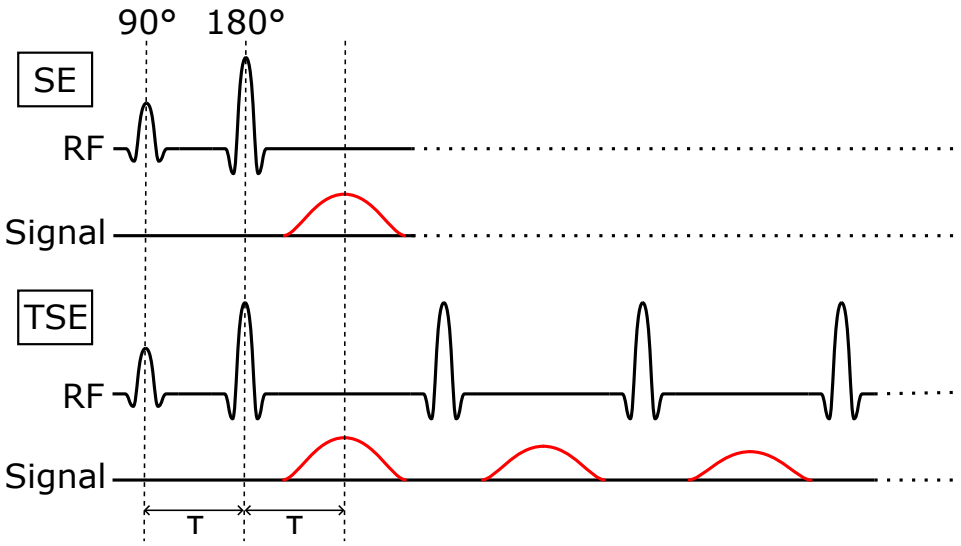

Figure C.1: Simplified sequence diagrams for a Spin Echo (SE) sequence and a Turbo Spin Echo (TSE) sequence. The SE sequence consists of a 90° excitation pulse and a 180° refocusing pulse, whereas the TSE sequence contains multiple refocusing pulses. The excitation pulse and the first refocusing pulse are separated by a time interval τ; the first echo therefore occurs at $TE = 2\tau$. The echoes for both sequences are shown in red. The TSE sequence makes more efficient use of the time between the repetitions, but the signal decreases for subsequent echoes.

quired. In this way, multiple k-space lines can be acquired during a single repetition, causing a significant speedup. This speedup is proportional to the Echo Train Length (ETL) or TSE factor.

TSE sequences have multiple parameters that can be optimized. The ETL is one of these parameters: a high ETL results in faster imaging, but the signal for the last echoes will be low. An ETL that is chosen too high will therefore result in images with bad contrast. Additionally, the decaying signal imposes a filter in k-space, and an ETL that is too high may therefore also lead to blurring in image space. The flip angles for the RF pulses can be adjusted as well [36]. In the simplest case, the excitation pulse has a flip angle of 90° and all refocusing pulses have a flip angle of 180°. Choosing a lower value for the refocusing pulses, e.g. 60°, generates stimulated echoes. This slows down the signal decay for a longer period of time, and therefore allows for a higher ETL. It is also possible to use different flip angles for the refocusing pulses. In this way, the signal can be kept constant for a short period of time, thus minimizing k-space blurring. It should be noted that this is only possible for a single combination of longitudinal and transverse relaxation times. Lastly, an important parameter is the k-space filling order, illustrated in Figure C.2. Sequential filling of k-space lines results in a sawtooth-like amplitude variation, which can cause artifacts and blurring of the image. Interleaved filling results in a smoother amplitude variation in k-space, which reduces these effects [37, p. 784]. More complex filling orders are also possible [36]. An important aspect of the filling order is the ability to choose at which moment the center of k-space is sampled. This is a determining factor for the image contrast.

C.2. Extended Phase Graphs

Although it is possible to optimize these parameters by trial and error, it is more practical and less time-consuming to start with simulations. A commonly used tool for the simulation of TSE sequences are Extended Phase Graphs (EPG) [38]. EPG operates on the complex components of the magnetization,

$$\begin{aligned} M_+(\mathbf{r}) &= M_x(\mathbf{r}) + iM_y(\mathbf{r}) = (M_-)^* \\ M_-(\mathbf{r}) &= M_x(\mathbf{r}) - iM_y(\mathbf{r}) = (M_+)^* \end{aligned} \tag{C.1}$$

Where M_+ and M_- can be interpreted as two transverse components rotating in opposite directions. Over

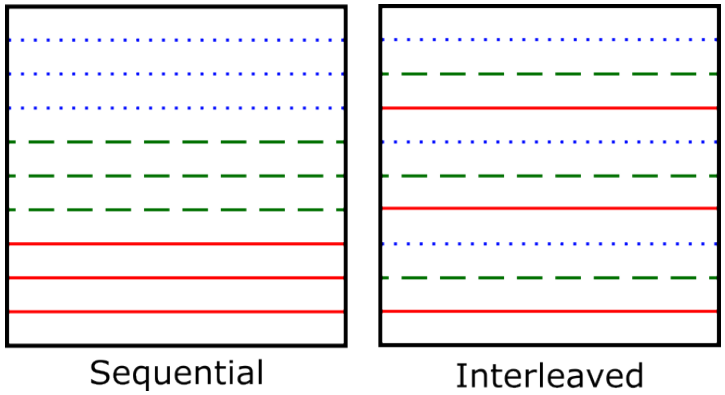

Figure C.2: Two different k-space filling orders. Left: sequential filling; right: interleaved filling. Each color indicates a set of k-space lines acquired during a single repetition. In this example, the ETL is 3. Sequential k-space filling causes amplitude jumps in k-space, due to transverse relaxation. Interleaved k-space filling results in a smoother amplitude gradient [37, p. 784].

time, the spins acquire different phases, which need to be simulated separately. Keeping track of all different spins with different phases becomes complex, even for simple simulations. Therefore, instead of using the magnetisations directly, EPG works with a Fourier representation of these components:

$$\begin{aligned} \tilde{F}_-(\mathbf{k}) &= \int_V M_-(\mathbf{r}) e^{-i\mathbf{kr}} d^3r \\ \tilde{F}_+(\mathbf{k}) &= \int_V M_+(\mathbf{r}) e^{-i\mathbf{kr}} d^3r \\ \tilde{Z}(\mathbf{k}) &= \int_V M_Z(\mathbf{r}) e^{-i\mathbf{kr}} d^3r \end{aligned} \tag{C.2}$$

This Fourier basis allows to keep track of many spins using a single state. A state is represented by a single value of $\mathbf{k}$. In the most basic version of EPG, only discrete values of $\mathbf{k}$ are used, i.e. $\mathbf{k} = \ldots, -3, -2, -1, 0, 1, 2, 3, \ldots$. States with $k \neq 0$ are assumed to be fully dephased, and thus do not contribute to the signal. In EPG, the full system is described by a state matrix, which contains two transverse states ($\tilde{F}$) and one longitudinal state ($\tilde{Z}$):

$$\Omega = \begin{bmatrix} \tilde{F}_+(0) & \tilde{F}_+(1) & \tilde{F}_+(2) & \ldots \\ \tilde{F}_-(0) & \tilde{F}_-(-1) & \tilde{F}_-(-2) & \ldots \\ \tilde{Z}(0) & \tilde{Z}(1) & \tilde{Z}(2) & \ldots \end{bmatrix} \tag{C.3}$$

The elementary actions in a pulse sequence, e.g. RF pulses, relaxation and gradients, are described as matrix operations on this state matrix. An RF pulse with flip angle α and phase ϕ is simulated using the transformation matrix $\mathbf{T}(\alpha, \phi)$:

$$\begin{bmatrix} \tilde{F}_+(k) \\ \tilde{F}_-(-k) \\ \tilde{Z}(k) \end{bmatrix}^+ = \begin{bmatrix} \cos^2\frac{\alpha}{2} & e^{2i\Phi}\sin^2\frac{\alpha}{2} & -ie^{i\Phi}\sin\alpha \\ e^{-2i\Phi}\sin^2\frac{\alpha}{2} & \cos^2\frac{\alpha}{2} & ie^{-i\Phi}\sin\alpha \\ -\frac{i}{2}e^{-i\Phi}\sin\alpha & \frac{i}{2}e^{i\Phi}\sin\alpha & \cos\alpha \end{bmatrix} \begin{bmatrix} \tilde{F}_+(k) \\ \tilde{F}_-(-k) \\ \tilde{Z}(k) \end{bmatrix}^- \tag{C.4}$$

Relaxation during a time interval τ is simulated by multiplying the state matrix with a relaxation matrix $\mathbf{E}$, which is defined as

$$\mathbf{E}(\tau, T_1, T_2) = \begin{bmatrix} E_2 & 0 & 0 \\ 0 & E_2 & 0 \\ 0 & 0 & E_1 \end{bmatrix}, \tag{C.5}$$

where E_1 and E_2 are the longitudinal and transverse relaxation terms, which are defined as $E_{\{1,2\}} = \exp -\tau/T_{\{1,2\}}$. This operator only includes decay, but the longitudinal magnetisation also experiences regrowth. To incorporate this in the simulations, a slightly different relaxation operator is used for the $\mathbf{k} = 0$ state:

$$\begin{bmatrix} \tilde{F}_+(0) \\ \tilde{F}_-(0) \\ \tilde{Z}(0) \end{bmatrix}^+ = \begin{bmatrix} E_2 & 0 & 0 \\ 0 & E_2 & 0 \\ 0 & 0 & E_1 \end{bmatrix} \cdot \begin{bmatrix} \tilde{F}_+(0) \\ \tilde{F}_-(0) \\ \tilde{Z}(0) \end{bmatrix}^- + \begin{bmatrix} 0 \\ 0 \\ M_0\,(1 - E_1) \end{bmatrix} \tag{C.6}$$

Finally, dephasing is defined as a simple shift.

$$S(\Delta\mathbf{k}) : \tilde{F}_\pm(\mathbf{k}) \rightarrow \tilde{F}_\pm(\mathbf{k} + \Delta\mathbf{k});\ \tilde{Z}(\mathbf{k}) \rightarrow \tilde{Z}(\mathbf{k}) \tag{C.7}$$

In (C.7), all transverse states are shifted by $\Delta\mathbf{k}$. Note that the longitudinal states are not shifted, since these states do not dephase. Z-states can therefore only be created by applying RF pulses [38].

C.3. Simulating multiple repetitions of a TSE sequence

Simulating a TSE sequence with EPG is fairly straightforward; a good example is provided in [38]. In the simulations, the excitation pulse of this sequence has a phase of 90°, according to the CPMG conditions. The refocusing pulses have a phase of 0°. During each half echo spacing τ, a shift of $\Delta\mathbf{k} = 1$ occurs, i.e. the transverse states are shifted up by one state.

In practice, it can be useful to include a few dummy repetitions prior to acquiring the image. During these dummy repetitions, the signal may still vary between the repetitions. The goal of these dummy repetitions is to bring the system in an equilibrium situation. Surprisingly, the 'standard implementation' of EPG provided by Weigel implements only a single repetition, and adding multiple repetitions to their code is not straightforward. It was therefore necessary to write our own code, which was initially done using Sycomore, a Python MRI simulation toolkit [39]. In order to assess the effect of multiple repetitions, the sequence was simulated multiple times, and each repetition started with the state matrix resulting from the previous repetition. The result of this simulation for a simple TSE sequence is shown in C.3. A 90°-pulse is used for excitation and 180°-pulses are used for refocusing. The ETL is 30, the echo spacing is 10 ms, and the number of repetitions is 10; relaxation effects are ignored. In this case, the first repetition is expected to give a very strong signal. After the first repetition, the transverse magnetization should be spoiled, and no regrowth should occur, because there is no relaxation. All subsequent repetitions will therefore give no signal, which can be considered the equilibrium situation. However, the results of this simulation are unexpected: the system does not reach an equilibrium after the first few repetitions, but shows sudden 'jumps' in the signal amplitude instead. The jumps appear to be periodic and show a decreasing amplitude.

At first, the simulations were thought to contain an error, but this error could not be found. A second implementation of EPG was therefore written from scratch; the results of these simulations displayed the same behaviour. An explanation for this behaviour was found by drawing the EPG diagrams for a very simple TSE sequence, ignoring relaxation effects. The mechanism behind the jumps is analogous to that behind a stimulated echo. At the end of the first repetition, the state $\tilde{F}_+(1)$ is occupied (Figure C.4 A); after the excitation pulse of the second repetition, a part of this transverse magnetisation is converted to $\tilde{F}_-(1)$ (Figure C.4 B). At the end of the second repetition, this transverse magnetisation is rephased, i.e. $\tilde{F}_+(0)$ is occupied. The excitation pulse of the third iteration stores this transverse magnetisation as in-phase longitudinal magnetisation in $\tilde{Z}(0)$ (Figure C.4 C). This state remains unchanged during the third repetition. In the fourth repetition, the excitation pulse flips the longitudinal magnetisation back into the transverse plane ($\tilde{F}_+(0)$), where it causes an echo-forming pathway (Figure C.4 D).

It can thus be concluded that the signal jumps are caused by the spin history. However, this does not reflect what one would expect during real measurements. In real life, the signal causing the jumps would be spoiled before every new repetition. It is therefore necessary to include spoiling in the simulations.

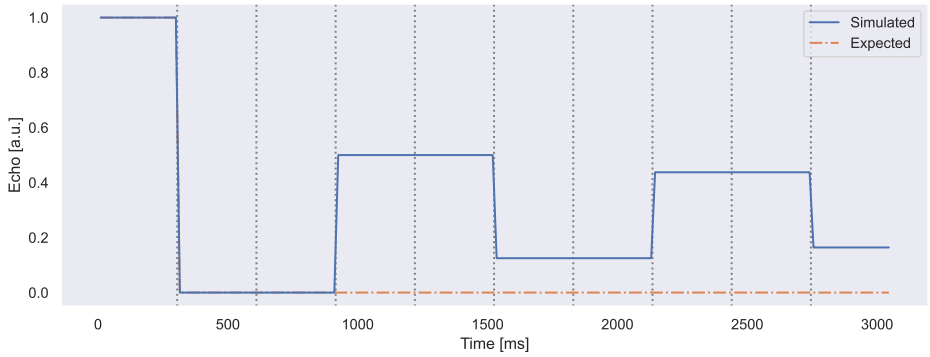

Figure C.3: Simulated and expected signal for 10 repetitions. The repetitions are separated by grey, dashed lines. Although this sequence is expected to only give a signal during the first repetition, the simulated signal shows periodic jumping behaviour.

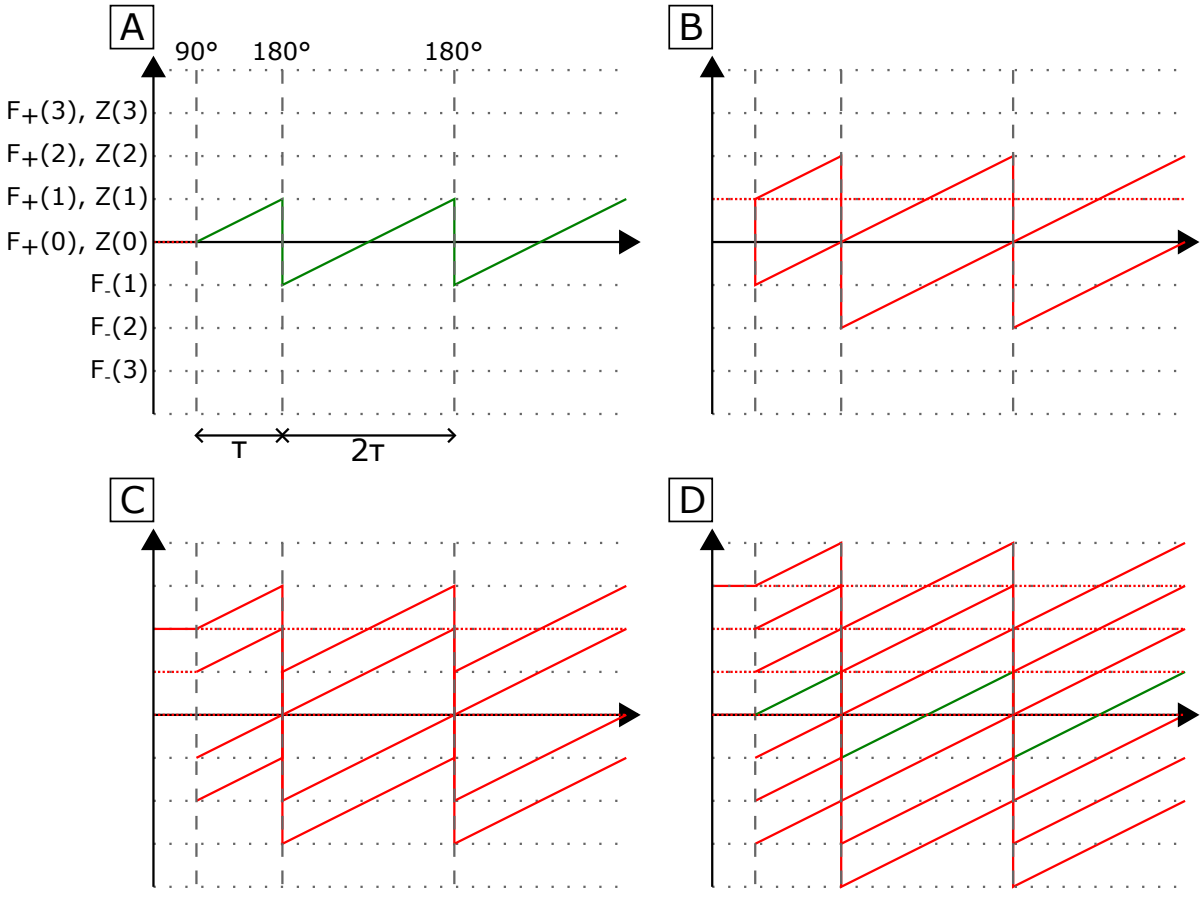

Figure C.4: EPG diagram for multiple repetitions of a basic TSE sequence, consisting of a 90° excitation pulse and two 180° refocusing pulses. Vertical, grey dashed lines indicate the RF pulses; horizontal grey dotted lines indicate the different states. Echo forming pathways are coloured green; other pathways are coloured red. Transverse states are indicated by a solid line, whereas longitudinal states are drawn using a dotted line. Relaxation effects are completely ignored in this diagram, so the echo forming pathway in the fourth repetition (D) is entirely caused by spin history.

C.4. Simulating a spoiled TSE sequence

Various spoiling methods exist. The most used spoiling method, RF spoiling, makes use of RF pulses with different phases [24, p. 505]. However, since the CPMG conditions [40] impose strict conditions on the phase of the RF pulses, this method cannot be used in our simulations. Another well-known method is gradient spoiling, which dephases the transverse relaxation using gradients [24, p. 506]. In practice, gra-

dient spoiling can be incorporated in a TSE sequence by applying a very strong gradient at the end of each repetition. Imperfections in the gradient field will cause incoherent behaviour, preventing the spins from rephasing later on. In our simulations, however, the gradients are ideal, and the resulting behaviour will be coherent. The dephased spins will therefore rephase again, and still cause the jumps in the signal. This is visible in the simulations shown in Figure C.5. Furthermore, ringing-like behaviour is visible at the end of each repetition: the signal suddenly increases during the last few pulses. Incoherence could be simulated by randomising the gradient strength after each repetition, but this causes issues with the reproducibility of the simulations.

Spoiling can also be simulated by directly modifying the phase graph, for example by discarding certain states. In practice, spoiling eliminates the transverse magnetisation, which can be simulated by discarding all transverse states ($F_\pm$). This does not solve the jumping and ringing behaviour, as can be seen in Figure C.5. In fact, from Figure C.4 can be concluded that the jumping behaviour will occur as soon as a transverse state $F_\pm(\mathbf{k} > 0)$ exists at the start of a repetition. This is the case when there is a dephased longitudinal state $Z(\mathbf{k} > 0)$ at the end of the previous repetition; discarding the longitudinal states only is therefore not sufficient to solve the observed problems. Another approach is to discard all states except $\tilde{Z}(0)$; this means only the in-phase longitudinal magnetisation survives the repetition. The results for this method are as well shown in Figure C.5; the jumping and ringing behaviour does indeed not occur anymore. This seems therefore a suitable method to simulate spoiled TSE sequences using EPG.

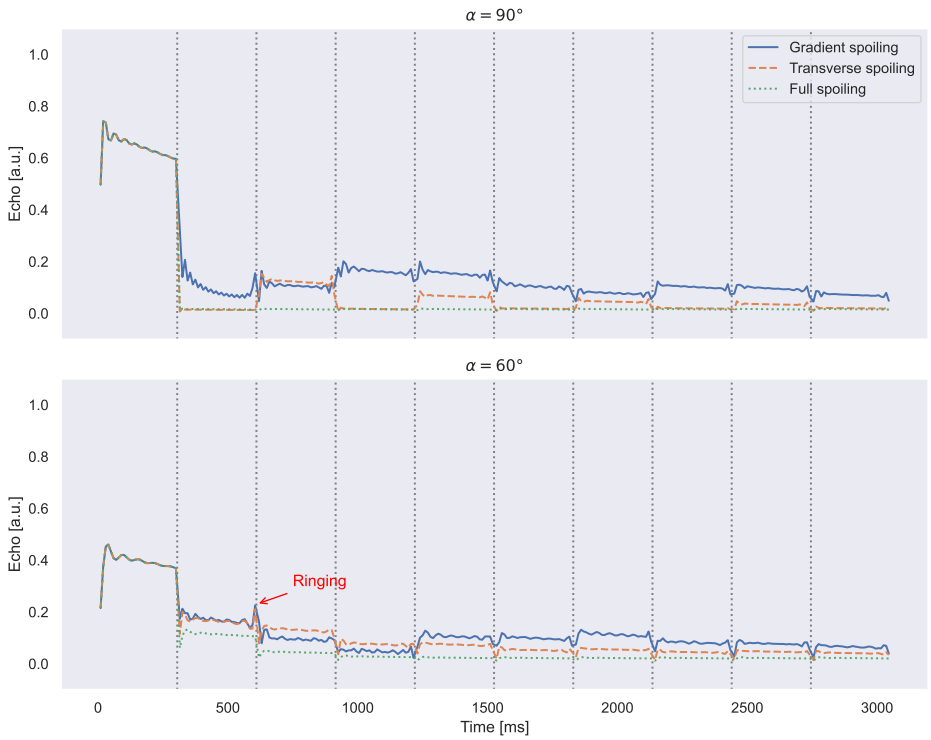

Figure C.5: Signals simulated using various spoiling implementations. The sequence is largely equal to the sequence used in Section C.2, with spoiling after each repetition. In this case, relaxation effects were not ignored; instead, the simulations were performed using $T_1 = 3500$ ms and $T_2 = 1500$ ms. Furthermore, refocusing pulses of 90° (top) and 60° (bottom) were used, because some problems do not occur for refocusing pulses of 180°. Three different implementations for spoiling were used. For *gradient spoiling*, a phase shift of $\Delta\mathbf{k} = 7$ was applied at the end of each repetition. This still results in the jumping and ringing-like behaviour. *Transverse spoiling* means that the transverse states are discarded at the end of each repetition; this does not solve the problems mentioned before. For *full spoiling*, all states except $\tilde{Z}(0)$ are discarded, which does indeed solve these problems. Unlike the other two methods, this method results in an equilibrium situation after a few repetitions.

C.5. Remaining questions

Simulating spoiled TSE sequences using EPG by discarding all states except $\tilde{Z}(0)$ solves the problems observed in simulations using other spoiling methods. However, this does not mean that this is a correct way to simulate spoiling. Discarding the transverse states can be justified by the fact that the goal of spoiling is to eliminate the transverse magnetisation, but this is less clear for discarding dephased longitudinal states ($Z(\mathbf{k} > 0)$). On one hand, the fact that they are longitudinal states suggests that they should not be affected by spoiling. On the other hand, the physical interpretation of dephased longitudinal states is unclear, and maybe they can only exist in combination with a dephased transverse state. In this case, spoiling would affect both transverse and longitudinal states, which justifies the spoiling method proposed here. In conclusion, discarding all states except $\tilde{Z}(0)$ seems to be an appropriate method to simulate spoiling in EPG, but a clear, physical understanding of the $Z(\mathbf{k} > 0)$ states is necessary in order to verify this.

D

Supplementary figures

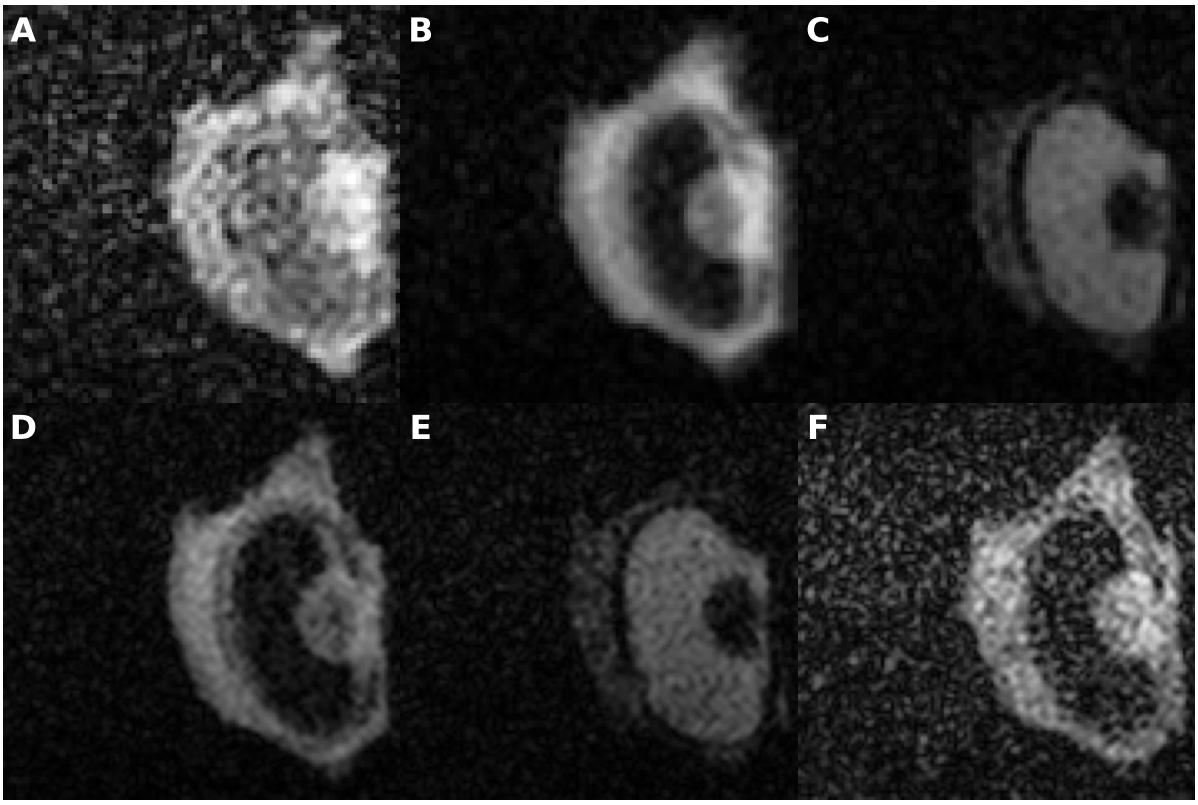

Figure D.1: Images of a porcine eye, acquired with the six sequences listed in Table 3.3. All images display the center slice of the scans, in the transverse plane; the vertical axis is the readout axis. All images are displayed with the same intensity range. The image order is the same as in Figure 4.3.

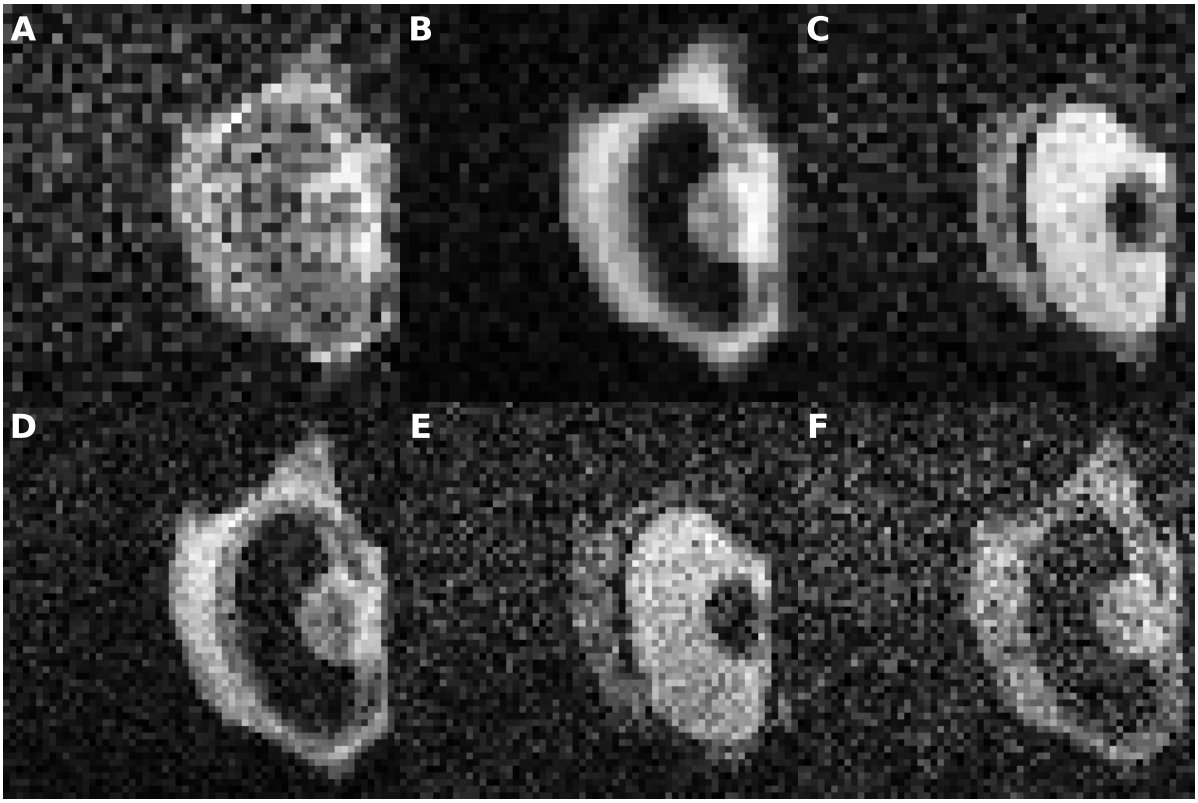

Figure D.2: Images of a porcine eye, acquired with the six sequences listed in Table 3.3. All images display the center slice of the scans, in the transverse plane; the vertical axis is the readout axis. The intensity ranges of these images are independent. These images show that the SNR in the T_2-weighted images (**C, E**) is lower than in the corresponding T_1-weighted images (**B, D**). Furthermore, the SNR in the higher resolution images (**B, C**) is lower than the SNR in the lower resolution images (**D, E**).